NATIONAL AERONAUTICS AND SPACE ADMINISTRATION

Technical Memorandum 33-493

Flexible Spacecraft Control System Design Procedures Utilizing Hybrid Coordinates

P. W. Likins
E. L. Marsh
G. E. Fleischer

JET PROPULSION LABORATORY
CALIFORNIA INSTITUTE OF TECHNOLOGY
PASADENA, CALIFORNIA

September 15, 1971

NATIONAL AERONAUTICS AND SPACE ADMINISTRATION

Technical Memorandum 33-493

Flexible Spacecraft Control System Design Procedures Utilizing Hybrid Coordinates

P. W. Likins
E. L. Marsh
G. E. Fleischer

JET PROPULSION LABORATORY
CALIFORNIA INSTITUTE OF TECHNOLOGY
PASADENA, CALIFORNIA

September 15, 1971

Prepared Under Contract No NAS 7-100
National Aeronautics and Space Administration

PREFACE

The work described in this report was performed by the Guidance and Control Division of the Jet Propulsion Laboratory.

CONTENTS

Introduction 1

Design Procedures 2

Appendix A. An Idealized Test Vehicle 8

Appendix B. The TOPS Autopilot 21

Appendix C. The Attitude Control of a Flexible Solar Electric Spacecraft 32

TABLES

1. Mode shapes and frequencies 12

2. TOPS hybrid-coordinate structural model data 26

FIGURES

1. Idealized test vehicle 9

2. Mode shapes for test vehicle 11

3. Test vehicle root locus for lead-lag control with remote complex poles 16

4. Test vehicle root locus for lead-lag control with near complex poles 17

5. Test vehicle root locus for lead-lag-lag control with complex poles 18

6. Two-mode flexible test vehicle root locus for lead-lag-lag control 19

7. Thermoelectric outer planet spacecraft 22

8. Linearized and simplified yaw autopilot loop 24

9. TOPS autopilot yaw axis root locus 29

10. TOPS autopilot pitch axis root locus 30

11. Stability diagram 31

12. Yaw axis response, rigid vehicle, $K_x = K_y = 2.2$ 33

13a. Yaw axis response, flexible vehicle, $K_x = K_y = 2.2$ 34

13b. Yaw axis response, flexible vehicle, $K_x = K_y = 1.0$ 34

FIGURES (contd)

14. Solar electric spacecraft 35
15. Engine cluster 36
16. Translator 38
17. Solar array mode shapes 55
18. Linear approximation to the control system block diagram 58
19. Coupled three-axis block diagram 59
20. $\underline{b}_1$ axis block diagram 61
21. $\underline{b}_2$ axis block diagram 62
22. $\underline{b}_3$ axis block diagram 63
23. $\underline{b}_1$ axis root locus, fourth and fifth mode flexibility 69
24. $\underline{b}_1$ axis root locus 71
25. $\underline{b}_2$ axis root locus, first mode flexibility 72
26. $\underline{b}_2$ axis root locus, rigid vehicle 73
27. $\underline{b}_3$ axis root locus, second mode flexibility 74
28. θ_1 response, $K_{S1} = 20.0$ 76
29. θ_2 response, $K_{S2} = 100.0$ 77
30. θ_3 response, $K_{S3} = 100.0$ 78
31. θ_1 response, $K_{S1} = 50.0$ 79
32. θ_2 response, $K_{S2} = 350.0$ 80
33. θ_3 response, $K_{S3} = 350.0$ 81

ABSTRACT:

Procedures for the practical implementation of the hybrid coordinate methods of dynamic analysis of flexible spacecraft in application to vehicles of realistic complexity are briefly documented, with supporting examples.

INTRODUCTION:

Reference 1 provides a detailed derivation of equations representing the dynamic behavior of spacecraft idealized as collections of rigid bodies and flexible appendages; these equations employ a hybrid system of coordinates, including discrete coordinates for rigid bodies and distributed or modal coordinates for elastic appendages. The objective of Reference 1 is the development and dissemination of a body of theory, with only minimal consideration being given to the ways in which this material might be used.

In the period following the preparation of Reference 1, serious attention has been given at JPL to the development of the practical utility of the hybrid coordinate method by exploration of the various ways in which it can be used in the practical design of attitude control systems for flexible spacecraft. The application of hybrid coordinate design procedures to specific spacecraft has been described in separate papers as these methods have evolved (References 2,3); the present report is a compilation and documentation of the present status of this continuing process of developing and refining design tools which have become available only with the introduction of the hybrid coordinate method of Reference 1.

It may be remarked that the hybrid coordinate method has been widely adopted outside of JPL, and in project applications design procedures have evolved in other organizations. This Memorandum is however largely confined to those design methods developed and applied within JPL.

Detailed technical material is reserved in this Memorandum for three appendices, each treating a specific example. The emphasis in the body of this report is on the qualitative description of design procedures and the comprehensive strategy of approaching the task of attitude control system design for spacecraft with large flexible components.

DESIGN PROCEDURES:

A feature of the hybrid coordinate formulation of equations of motion which distinguishes them from those obtained by the vehicle normal mode method is the retention in the former of explicit attitude variables for that rigid portion of the vehicle for which attitude control must be maintained. Because these variables (perhaps a set of three attitude

angles) remain explicitly in the equations, it is a simple matter when the equations are linearized to obtain a transfer function relating the transforms of these attitude variables to transformed control system torques, autopilot gimbal angles, or whatever measure of control system actuation is most convenient. The influence of vehicle flexibility, as reflected in the response of any number of flexible appendage modal coordinates, is manifested in the transfer functions for the attitude variables. Thus the hybrid coordinate method is particularly well-adapted to the many control system design procedures which employ transfer functions.*

At JPL, transfer functions have in the past been used primarily in the form of scalar (single-axis) transfer functions for the generation of root locus plots. A computer program developed by E. Kopf and R. Mankovitz permits rapid and inexpensive construction of root locus plots, which have proven to be extremely useful for preliminary design of flexible vehicle control systems (see Appendices A, B, C).

Other organizations (e.g. Hughes Aircraft Company) have used Reference 1 to obtain transfer functions which they have employed in generating phase-gain plots, and any of the other conventional alternatives to root-locus plots can equally well be utilized.

For a rigid body, the assumption of uncoupled single-axis response is

*This is not to say that transfer functions cannot be obtained from equations employing either exclusively discrete coordinates or exclusively modal coordinates, since any linear set of equations will suffice. If one requires transfer functions only for the vehicle attitude variables however, with deformation variables occupying a secondary importance, then transfer functions obtained from hybrid coordinate equations are both conceptually simpler and easier to calculate.

jeopardized only by the existence of products of inertia for the control axes or the presence of stored angular momentum normal to the control axis. For a flexible S/C, one must add to these considerations the likelihood that any given mode of vibration of a flexible appendage will also cause cross-axis coupling. Except for the simplest of idealized S/C (such as that in Appendix A), it must be expected that single-axis response studies for flexible S/C will be less valid in predicting vehicle response than has been the case with the nominally rigid S/C of the past. Whereas it has been a common past practice in S/C control system design to proceed directly from linearized, single-axis response studies using root locus plots to digital simulation of coupled, nonlinear equations, it is recommended that an intermediate step be inserted when vehicle flexibility is expected to introduce cross-axis coupling. This step involves the analysis of coupled equations for which the approximations of linearization have been retained.

The use of transfer functions does not preclude the incorporation of cross-axis coupling, but such coupling does complicate their use as a design tool. One can select one of the three axes (say axis 1), and establish a control law for the torque T_1 about this axis to maintain control of the corresponding attitude angle θ_1; and then proceed to the second axis and devise a control law for T_2 with the recognition that θ_2 is influenced not only by T_2 but also by T_1, which is introduced according to the control law as a consequence of the θ_1 induced by T_2. By the time one faces the prospect of choosing a control law for T_3 to control θ_3, the influences on θ_3 of T_1 (available as a function of θ_1) and T_2

(available as a function of θ_2) greatly complicate the design task, and the designer may wonder if his job would have been easier had he started with the 3-axis; but there are no conceptual obstacles to this approach.

At JPL the problem of analyzing coupled linear equations has been confronted directly with a digital computer program for the determination of eigenvalues and eigenvectors, eschewing coupled-axis transfer functions. After the investment of some effort in obtaining a suitable eigenvalue-eigenvector program and acquiring the necessary skills in its use*, this has become a useful design tool for flexible vehicle attitude control systems. In Appendix C the results of eigenvalue studies for the TOPS vehicle are presented, and compared with preliminary conclusions based on single-axis response root locus studies.

The final analytical and computational step in control system design is a computer simulation of the system of coupled, nonlinear equations of motion; at JPL this step has been taken via digital computer numerical integration (see Appendices B and C).

Thus at JPL the design of attitude control systems for complex flexible spacecraft has evolved into a three-stage process: (1) Linearized single-axis response studies using computer-generated root locus plots, (2) Linearized coupled system equation studies using an eigenvalue-eigenvector computer program, and (3) Nonlinear coupled system simulations via digital computer.

*The program EVPEVT with error bound print-out was finally adopted, with the practice of normalizing variables to improve the conditioning of the input matrix until acceptable error-bounds were attained.

In each stage of analysis, appendage flexibility is represented in the hybrid coordinate approach by means of modal coordinates, and this would appear to require an extensive modal analysis of all flexible structure. This is a substantial mathematical modeling and computing task, involving the personnel and computer programs of a structures group. In the early phases of control system design, the structural design is generally also in a preliminary phase, and detailed modeling is unwarranted. This obstacle to efficient system design has been neatly circumvented by the development of an appreciation of the physical significance of certain matrices which embody the influence of appendage flexibility on control system design. Specifically, it has been noted that the influence of a flexible appendage in a given mode of vibration on control system operation can be characterized by a frequency σ, a damping ratio ζ, and the contribution of the mode to a matrix defined in Reference 1 at $\delta^T\delta$. This matrix has the units of moment of inertia, and represents (in a certain sense) the contribution of the flexible appendage to the vehicle inertia matrix. Although one must have a rough appreciation of the mode shape for a particular mode of vibration in order to estimate the contribution of that mode to $\delta^T\delta$, this estimate can be made in many cases without actually performing the modal analysis. For preliminary design pruposes it is therefore often possible simply to guess values of σ, ζ, and $\delta^T\delta$ for an hypothesized mode of appendage vibration. While such a guess will often require substantial revision as the vehicle design firms up and digital computer modal analysis becomes appropriate, this alternative is apt to be far preferable to the old practice of basing preliminary design on the

idealization of the vehicle as a rigid body.

As the design process converges, and fairly accurate characteristics of control system and structure can be ascertained, it becomes increasingly important that simulations incorporate those modes of appendage vibration which influence the control system. At the same time, there is ample motivation to exclude as many modes of vibration as possible from the simulation, due in general to the cost in computer running time of each additional coordinate, and in particular to the inordinately high cost in running time and computer accuracy of retaining high frequency modes of vibration.

In addition to the usual procedure of truncating modal coordinates by means of a frequency criterion, retaining only those modes with frequencies in the control system band-width, two more techniques have been developed at JPL for guiding truncation.

As noted previously, the contribution of a given mode to $\delta^T\delta$ is a measure of its influence on the attitude control system. This matrix should therefore be computed and printed out as part of the modal analysis task undertaken by the structural mechanics experts. It then becomes possible simply by inspection of the elements of a 3 x 3 matrix for each mode to determine the extent of its influence on control about a given control axis, and the degree to which it causes cross-axis coupling.

The final criterion for modal coordinate truncation in advance of digital computer numerical integration is the influence of an individual mode on system eigenvalues. It is much cheaper to explore the consequences of various alternative coordinate truncations with an eigenvalue program

than with a numerical integration routine.

It should be noted explicitly in this Memorandum that the hybrid coordinate method relies heavily upon the cooperative interaction of personnel in control systems and structural mechanics organizations. Not only are the structures people and their computer programs essential to the detailed task of appendage modal analysis, they also are invaluable in helping to formulate the rough estimates of σ, ζ, and $\delta^T\delta$ that go into preliminary control system design. At JPL there is a strong emphasis on promoting technical communication at the working level between individuals in Structural Mechanics (Division 35) and Guidance and Control (Division 34) and it is very important that this kind of joint effort be encouraged elsewhere. Larger aerospace organizations have on occasion been handicapped in their attempts to exploit the advantages of hybrid coordinate analysis by apparent difficulties in fostering continuing cooperative technical interaction between structures and controls groups.

APPENDIX A -- AN IDEALIZED TEST VEHICLE:

In order that the development of methods of control system design not be obscured by the mechanical complexity of the object being controlled, a simple, idealized test vehicle (Figure 1) has been devised to permit physically meaningful interpretation of all phases of the analysis. Figure 1 shows four elastic members attached to a rigid body B which may also contain a rigid, symmetric rotor. The elastic bodies are massless except for a tip mass on each, normalized to unity (weight .454Kg) The central body B (including its rotor) weighs (1.8Kg), so the vehicle mass is distributed equally between the rigid part and the four flexible attachments, which

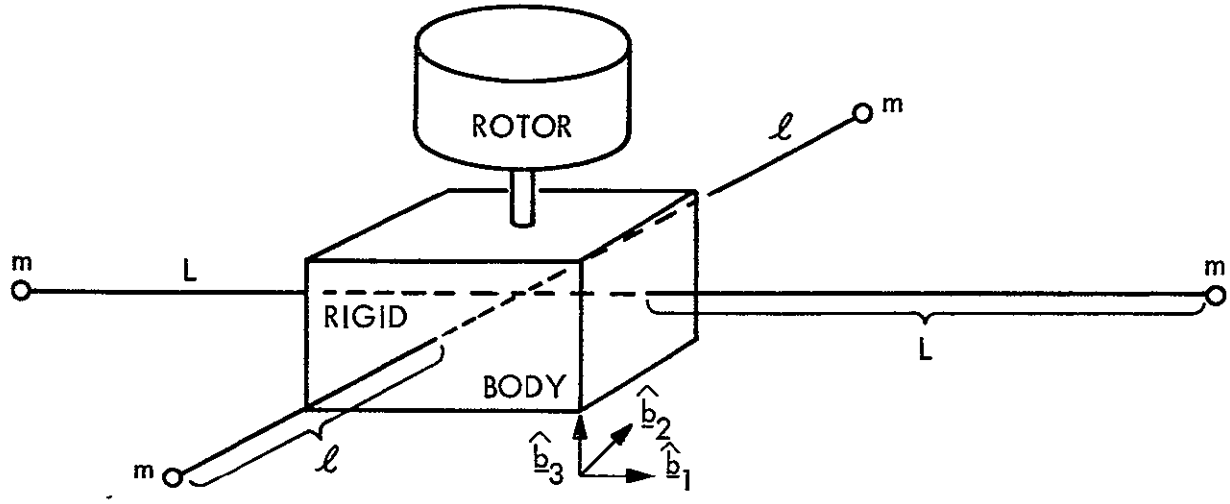

Figure 1. Idealized test vehicle

together comprise what will be called a single appendage. The tip masses are particles, and the central body is inertially spherical, with weight moment of inertia (.758 Kg-M^2) and dimensions small relative to beam lengths L and ℓ, chosen as (1.2m) and (.6m), respectively. Beam stiffnesses are chosen to make the long beams have natural frequencies of 0.90 and 1.81 Hz, respectively, in the 1-2 and 1-3 planes of the vehicle when attached to a stationary base B. The corresponding "cantilever mode" natural frequencies of the short beams are 2.71 and 4.52 Hz in the 1-2 and 2-3 planes, respectively. For the investigations reported in this appendix, all beams are assumed longitudinally inextensible.

The modal coordinates in the matrix $\overline{\eta}$ of Eqs. (224) and (216) of Reference 1 are not the cantilever modal coordinates of the individual beams, nor are they normal-mode coordinates of the total vehicle. (The

presence of the rotor makes the vehicle normal-modes complex, and these modes are not used here in order to confine the analysis to real numbers.) The coordinates in $\overline{\eta}$ establish the response of the appendage in modes in which they would vibrate freely if the rigid body was free in translation but constrained against rotation. With this interpretation, it becomes evident that there must be eight coordinates in the column matrix η, and for this simple system one can almost guess the mode shapes.

Using established digital computer eigenvalue-eigenvector routines, one can determine the eight natural frequencies and mode shapes quite accurately.* Results are presented schematically in Figure 2, and quantitatively in Table 1. In the latter, node numbers and numbers associated with "d.o.f." (degree of freedom) are to be obtained from the first diagram of Figure 2.

For purposes of preliminary design, it may be desirable to make exploratory transfer function calculations before the appendage is fully defined and subjected to modal analysis. Examination of the matrix transfer function in Eq. (292) of Reference 1 reveals that of the appendage properties only the matrices $\overline{\sigma}$, $\overline{\zeta}$, and $\overline{\delta}$ are required. The autopilot transfer function does involve other appendage properties (see Reference 3), but in the first approximation Equation (292) will suffice for autopilot control also. Since $\overline{\zeta}$ is actually assigned and not calculated, only $\overline{\sigma}$ and $\overline{\delta}$ must be calculated for application of the transfer function in this equation.

*Appreciation is expressed to Mr. John Garba of JPL, Division 35, who actually performed these computer operations, using the SAMIS program.

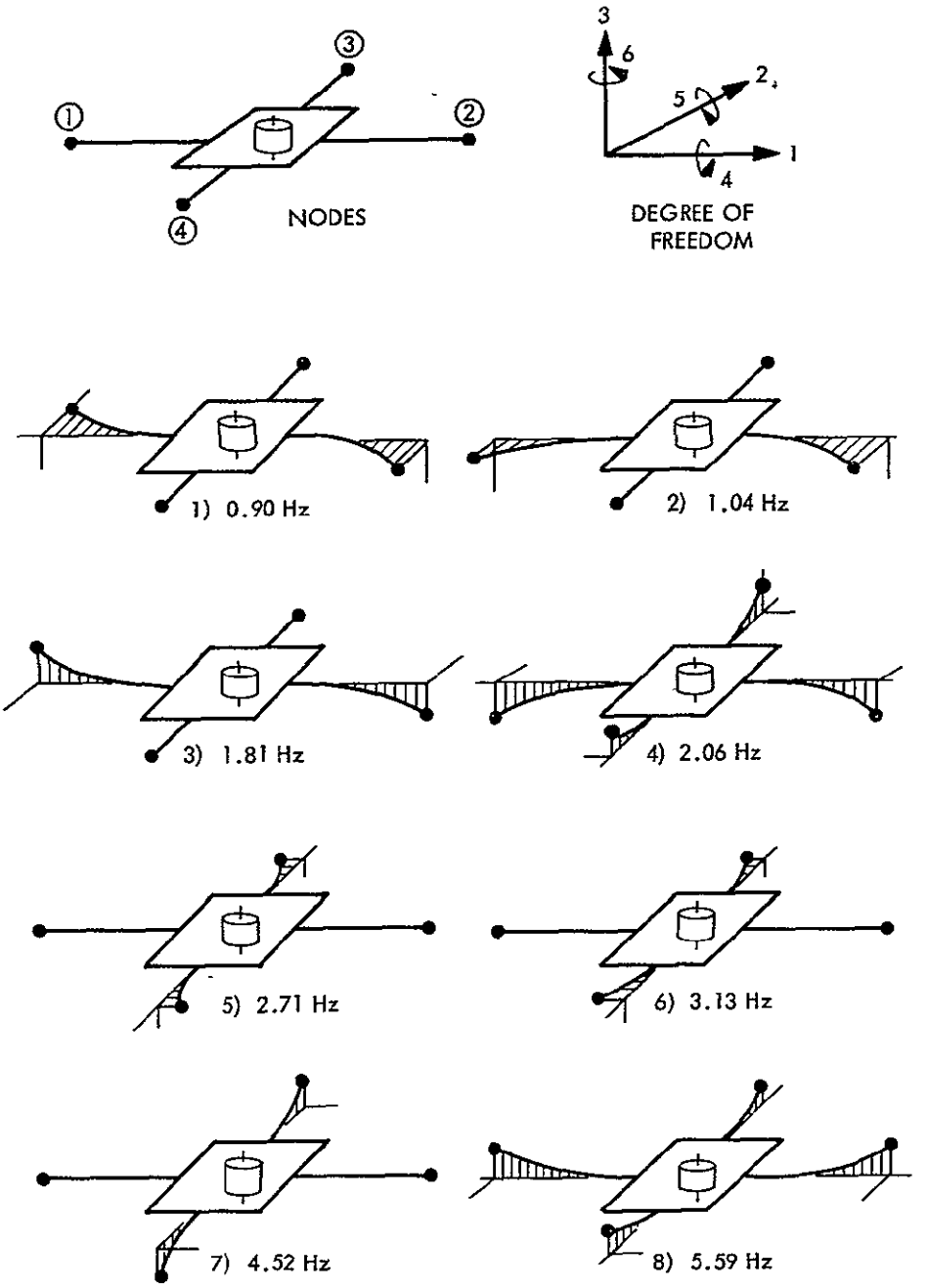

Figure 2. Mode shapes for test vehicle

Table 1. Mode shapes and frequencies

Node/d. o. f.	Mode				
	M1	M2	M3	M4	M8
1/2	0.707	-0.817	0	0	0
1/3	0	0	0.707	-0.799	0.335
1/5	0	0	0.022	-0.025	0.010
1/6	-0 022	0.026	0	0	0
2/2	-0.707	-0.817	0	0	0
2/3	0	0	-0.707	-0.799	0.335
2/5	0	0	0.022	0.025	-0 010
2/6	-0.022	-0.026	0	0	0
	M4	M5	M6	M7	M8
3/1	0	-0.707	-0.817	0	0
3/3	0.050	0	0	0.707	0.865
3/4	0.003	0	0	0.044	0.054
3/6	0	0.044	0.051	0	0
4/1	0	0.707	-0.817	0	0
4/3	0.050	0	0	-0.707	0.865
4/4	-0.003	0	0	0.044	-0.054
4/6	0	0.044	-0.051	0	0

For this simple system one can readily estimate $\sigma_1 \cong 0.9$ Hz, since this is the input cantilever mode natural frequency of the longest beams. Furthermore, one can utilize the physical interpretation of $\bar{\delta}^T\bar{\delta}$ offered in the previous section, and guess that in the first mode only the long beams will participate (as in Figure 2); $\delta_3^j\delta_3^j$ should therefore be given by $2(.454\text{Kg})(1.2\text{m})^2 \cong (1.35\text{Kg-m}^2)$, since this figure represents the contribution to I_3 of the two long beams. One might for this simple system easily guess as well the third, fifth, and seventh mode frequencies and contributions to $\bar{\delta}^T\bar{\delta}$, since these are asymmetric modes which have frequencies corresponding to the known cantilever mode frequencies. The physical interpretation of $\bar{\delta}^T\bar{\delta}$ tells us that the symmetric modes (modes 2, 4, 6, and 8 in Figure 2) contribute nothing to this matrix, so they can be completely ignored.

Confirmation of these estimates for frequencies and $\delta^{J^T}\delta^J$ contributions comes from the computer-generated value of $\bar{\delta}$, using the definition in Eq. (287) of Reference 1. The results for δ and $\delta^T\delta$ (with no truncation) are given by

$$\delta = \begin{matrix} 0 & 0 & -2a \\ 0 & 0 & 0 \\ 0 & 2a & 0 \\ 0 & 0 & 0 \\ 0 & 0 & a \\ 0 & 0 & 0 \\ a & 0 & 0 \\ 0 & 0 & 0 \end{matrix}$$

$$\delta^T\delta = \begin{matrix} b & 0 & 0 \\ 0 & 4b & 0 \\ 0 & 0 & 5b \end{matrix}$$

where a = (.01 Kg-m^2); b = (.34 Kg-m^2); and computer generated numbers below (3x10-9) have been replaced by zeros. (For unit consistency it must be noted that $\delta^T\delta$ is actually $\bar{\delta}^T E^{-1}\delta$, with E a unit inertia matrix.) For this simple system, the estimated values are entirely correct. (The predicted $\delta_3^1\delta_3^1$ = (1.35 Kg-m^2) checks (-1.16) squared, and the calculated $\delta^T\delta$ is precisely the contribution of the appendage masses to the vehicle inertia matrix. Furthermore, the even-numbered rows of δ are null, so these modes do not contribute to $\delta^T\delta$.)

Having obtained, by estimation or calculation, the necessary parameters of the flexible vehicle, the control system designer can begin the sequence of response analyses required for selection of a control system. In general, the first step might be the rapid construction of a number of root-locus plots for single-axis response, the second step might then be a series of eigenvalue studies for a smaller range of preliminary control system designs, and the final step would be a numerical integration of the most general system of equations of motion, to confirm the final control system design. For the simple test vehicle treated in this section, however, each appendage modal vibration contributes to the vehicle response about one axis only, so the three scalar equations of vehicle motion (Eq. 224 of Reference 1) are coupled only by the "gyroscopic coupling" of the rotor. Furthermore, response θ_3 about the $\hat{b}_3$ axis (See Figure 1) is completely uncoupled from responses θ_1 and θ_2 about axes $\hat{b}_1$ and $\hat{b}_2$, so root locus plots for this axis must indicate precisely the same response that would be obtained from eigenvalue calculations or numerical integrations. The purposes of this paper are best served by restricting the test vehicle

analysis results to the presentation of root locus plots for θ_3. In the next two appendices eigenvalue analyses and integration results are presented for space vehicles of realistic complexity.

Figures 3-6 portray root-locus plots for θ_3 response of the test vehicle, under various assumptions. The dashed-line loci on Figures 3-5 are based on the assumption that the vehicle is rigid, so they provide for three simple control systems a basis for evaluating the influence of flexibility. Figures 3-6 introduce flexibility in the first mode of vibration (see Figure 2 and Table 1). In this mode the normalized reduced inertia R_3^1 is $1 - (\delta_3^1 \delta_3^1 / I_3) = 1 - [1.35/(.76 + 1.68)] = 0.45$. The natural frequency σ_1 is 0.90 Hz, although in the plots this value is normalized to unity. The damping ratio ζ_1 is assumed to be 0.05 (a relatively high figure is chosen to improve the visual impact of the root locus plot). From Eq. (298) of Reference 1, the poles and zeros of the open-loop transfer function $G_3(s)$ may be obtained. With σ_1 normalized to unity, these roots become

$$P_{1,2} = 0,0 \qquad\qquad z_{1,2} = 0.05 \pm i$$

$$P_{3,4} = 0.111 \pm i\ 1.49$$

For Figure 3 the controller (feedback) transfer function $H_3(s)$ has a pair of complex poles, a real zero and a real pole of larger magnitude (so it might be called a lead-lag system with complex poles). The influence of flexibility on the locus is not surprising, but the "crossover gain" which marks the transition to instability is drastically reduced by the flexible appendage. Whereas a rigid vehicle would become unstable when the gain reaches 0.13, Figure 3 shows instability to result when the gain

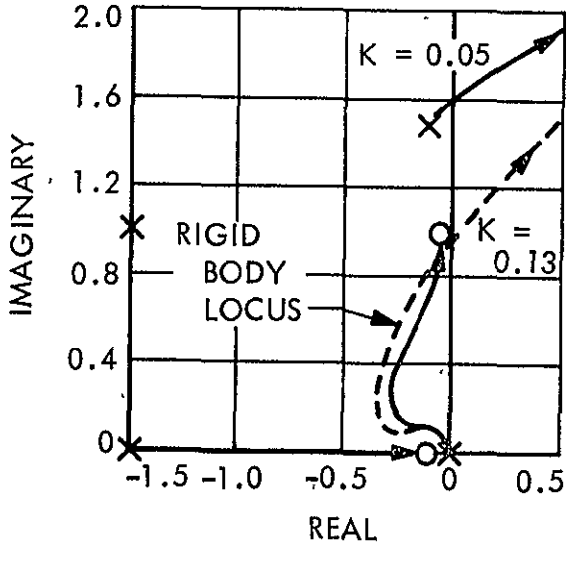

RIGID EFFECTS

4 OPEN-LOOP POLES

REAL	IMAG	ORDER
-1.5	0.0	1
-1.5	1.0	1
-1.5	-1.0	1
0.0	0.0	2

1 OPEN-LOOP ZERO(S)

REAL	IMAG	ORDER
-0.10	0.0	1

FLEXIBILITY EFFECTS

2 OPEN-LOOP POLES

REAL	IMAG	ORDER
-0.111	-1.49	1
-0.111	1.49	1

2 OPEN-LOOP ZERO(S)

REAL	IMAG	ORDER
-0.05	-1.0	1
-0.05	1.0	1

Figure 3. Test vehicle root locus for lead-lag control with remote complex poles

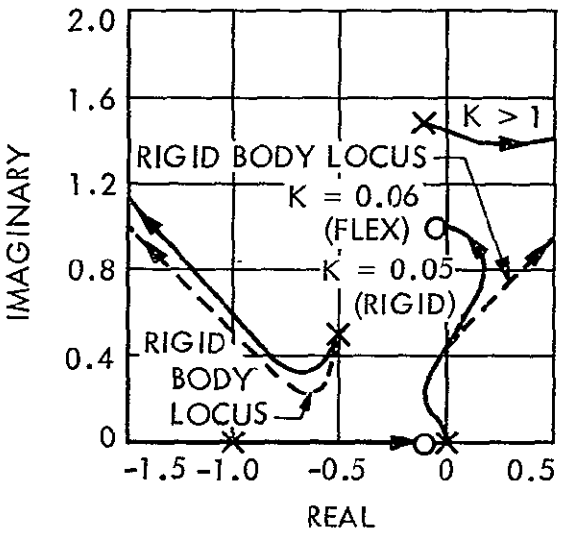

RIGID EFFECTS

4 OPEN-LOOP POLES

REAL	IMAG	ORDER
-1.0	0.0	1
-0.5	0.5	1
-0.5	-0.5	1
0.0	0.0	2

1 OPEN-LOOP ZERO(S)

REAL	IMAG	ORDER
-0.10	0.0	1

FLEXIBILITY EFFECTS

2 OPEN-LOOP POLES

REAL	IMAG	ORDER
-0.111	-1.49	1
-0.111	1.49	1

2 OPEN-LOOP ZERO(S)

REAL	IMAG	ORDER
-0.05	-1.0	1
-0.05	1.0	1

Figure 4. Test vehicle root locus for lead-lag control with near complex poles

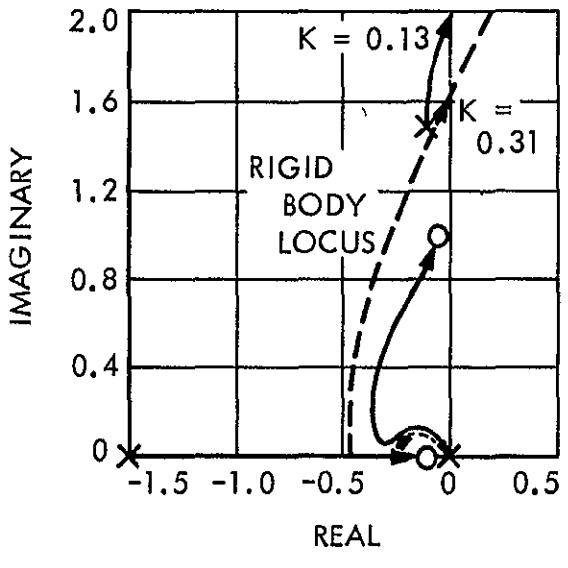

RIGID EFFECTS

3 OPEN-LOOP POLES

REAL	IMAG	ORDER
-1.5	0.0	1
-2.0	0.0	1
0.0	0.0	2

1 OPEN-LOOP ZERO(S)

REAL	IMAG	ORDER
-0.10	0.0	1

FLEXIBILITY EFFECTS

2 OPEN-LOOP POLES

REAL	IMAG	ORDER
-0.111	-1.49	1
-0.111	1.49	1

2 OPEN-LOOP ZERO(S)

REAL	IMAG	ORDER
-0.05	-1.0	1
-0.05	1.0	1

Figure 5. Test vehicle root locus for lead-lag-lag control with complex poles

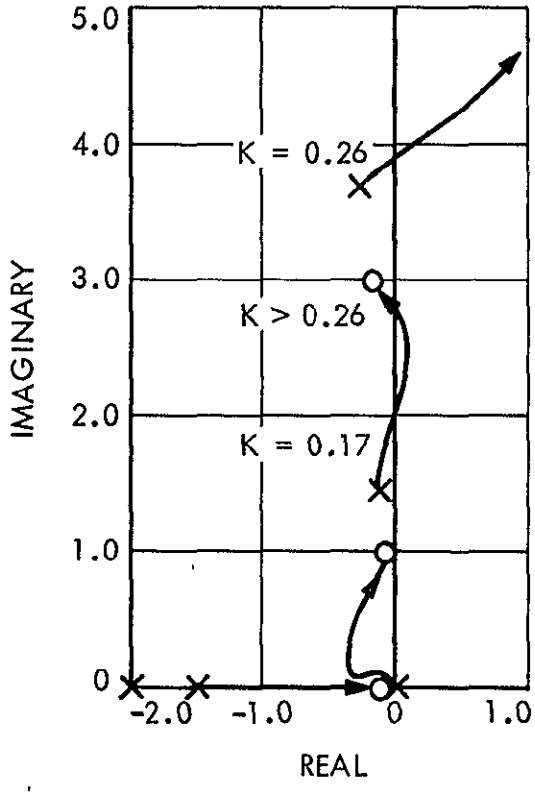

7 OPEN-LOOP POLES

REAL	IMAG	ORDER
-1.5	0.0	1
-2.0	0.0	1
0.0	0.0	2
-0.25273	-3.6948	1
-0.25273	3.6948	1
-0.10211	-1.4513	1
-0.10211	1.4513	1

5 OPEN-LOOP ZERO(S)

REAL	IMAG	ORDER
-0.10	0.0	1
-0.05	-1.0	1
-0.05	1.0	1
-0.15	-3.0	1
-0.15	3.0	1

Figure 6. Two-mode flexible test vehicle root locus for lead-lag-lag control

becomes 0.05. This is a reduction for the flexible vehicle to 38% of the cross-over gain for the rigid vehicle.

Parenthetically, it may be noted that the gain K employed in these root locus plots is related to the gain K' which appears as a factor in the feedback transfer function by a factor which is uninfluenced by the flexibility of a single mode. Thus changes in root locus plot gain K due to flexibility can be interpreted directly as changes in the actual feedback controller gain K'.

Figure 4 is, like Figure 3, based on a lead-lag control system with a pair of complex poles. The poles of $H_\alpha(s)$ in Figure 4 are somewhat closer to the original than in the previous example. The cross-over gain for the flexible vehicle appears to be 20% higher than for the rigid vehicle, whereas this gain is 62% lower when the complex pole of $H_\alpha(s)$ matches the structural frequency, as in Figure 3. Thus generalizations regarding the influence of appendage flexibility on control system stability would appear to be dangerous, and superficial physical interpretations unwise.

Figure 5 portrays the rigid vehicle response to a "lead-lag-lag" controller, with a negative real zero and two more remote negative poles (one of which is off the plot at -2.0). The cross-over gain is K = 0.31. Figure 5 illustrates the influence of the first mode flexibility of the appendage, which reduces the cross-over gain to 0.13, 42% of its original value. Figure 6 indicates the influence of the first and second modes of appendage vibration in combination.

For a "pure gain" direct feedback control, root-locus plots (not shown) can be deduced by inspection. It can be established by use of the Routhian

array that such control systems cannot be destabilized by appendage flexibility. (See Ref. 1, pp. 72-74 for details.)

For this idealized test vehicle there were generated 35 root locus plots, of which those preceding are typical. With a standardized program (written by E. H. Kopf and R. Mankovitz), each plot required only 10 to 40 sec of IBM 7094 time, depending on the number of plots requested in a given run. For the single-axis linear response of a vehicle as simple as this test vehicle, the conclusions are quantitatively precise. For a vehicle of realistic complexity (as treated in subsequent appendices), root locus plots may lose quantitative validity, while preserving the qualitative significance normally sought in preliminary design studies.

APPENDIX B -- THE TOPS AUTOPILOT:

The Thermoelectric Outer Planet Spacecraft (TOPS) configuration (Figure 7) is dominated by a (4.27m) diam parabolic communications antenna and a bank of radioisotope thermoelectric generators (RTGs). In addition, a pair of telescoping booms are required to provide separation for sensitive instruments (magnetometers, plasma wave detector, etc.). Much of the remaining scientific instrumentation has been provided viewing area (around the antenna) and separation from RTG radiation by mounting it on a large foldout structure opposite the RTG foldout boom. Finally, central to the craft is an electronic equipment compartment carrying the autopilot's attitude sensors (high-gain gyros) and actuator (gimbaled engine). It is this portion of the vehicle that will be considered the rigid body to which the flexible appendages (RTG, science, and magnetometer booms; antenna) are attached.

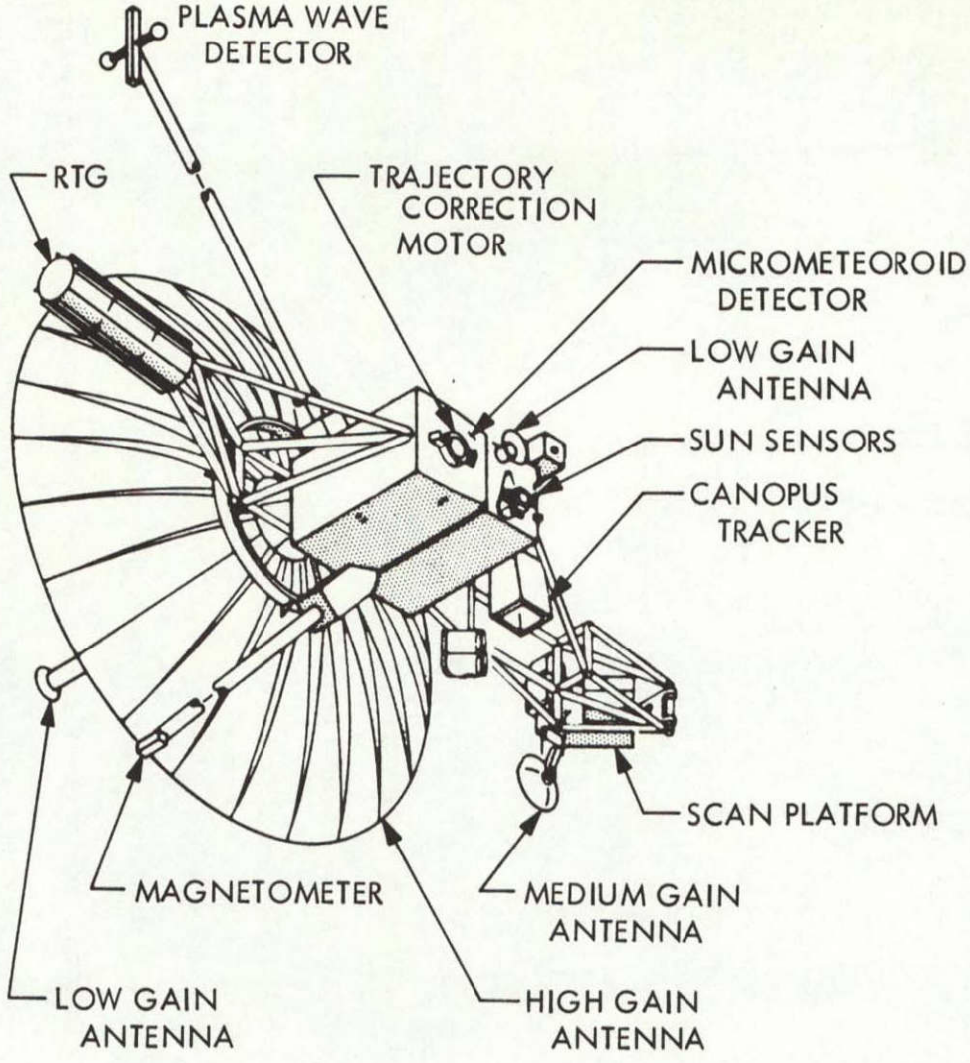

Figure 7. Thermoelectric outer planet spacecraft

While the hybrid coordinate formulation is also the ideal approach for the TOPS cruise attitude control system because of the use of momentum wheels, the discussion here is limited to initial investigations of the autopilot which maintains vehicle attitude during the trajectory correction motor's thrusting periods. The gimbaled engine provides attitude control about the pitch and yaw axes, while roll control is maintained by the roll gas jets, which, in the cruise control mode, are normally used to desaturate the roll wheels. Pitch, yaw, and roll momentum wheels are switched out during the trajectory correction phase along with their respective cruise optical sensors. Rate and position sensing is provided in all three axes by high-gain, rate-integrating gyros.

Preliminary efforts have attempted to determine the feasibility of using an autopilot control loop originally designed for a Mars orbital vehicle on TOPS as well. A linearized and simplified version of the proposed autopilot yaw axis (or pitch) loop is shown in Figure 8. Among the assumptions made to develop the simple, single-axis system model was that gimbaled engine reaction torques on the craft would not be considered, i.e., the engine is assumed massless. Also, as discussed previously, the influence on θ (pitch or yaw) of constant thrust along the vehicle roll axis is ignored; only the effects of the torque applied by the gimbaled motor and the resulting rigid-flexible body interactions are included.

Of course, the three-stage design process to be executed for the TOPS autopilot system must be based on the existence of a detailed hybrid coordinate structural model of the craft pictured in Figure 7. Such a model was developed* relatively quickly (2 weeks) using 20 discrete sub-bodies to

*Thanks must go to Messrs. Robert Bamford and Craig Helberg of Division 35 who modeled the structure and performed the necessary computer calculations.

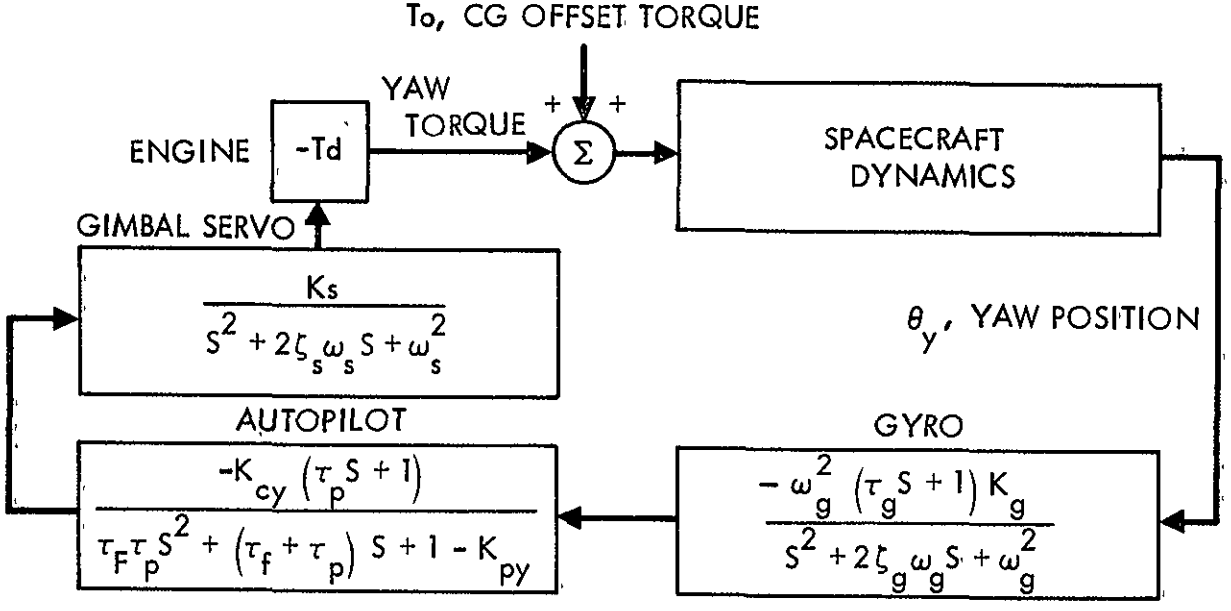

Figure 8. Linearized and simplified yaw autopilot loop

approximate the flexible members. The result of computer calculations to transform the discretized structural model into hybrid coordinate modal data is summarized, in part, in Table 2. Shown are the first ten modal frequencies obtained and corresponding elements of the matrices δ and $\phi^T M \Sigma_{EO}$. Approximately 30 modes were available in all from the computer generated data.

It is at this stage that one must begin to weigh the importance of the modes and, tentatively at least, truncate the modal data. The first five modes, grouped near 1 Hz may be traced to the antenna and magnetometer booms. One can see from the size of coefficients in δ that pitch and yaw axes are predominantly affected by modes 1 and 4 while roll largely sees modes 2, 3, and 5. Based on very simple modeling of the craft as a rigid body hinged to two rigid booms, natural frequencies of vibration above 4 Hz were shown to have little effect on autopilot stability. Therefore modes beyond 5 were removed from the dynamic model for all phases of the analysis including the detailed computer simulation. An additional excuse for deleting the significantly higher frequency modes is the dramatic improvement in numerical integration speed if digital simulation is employed.

Equation (298) of Reference 1 can now be of use in examining the linearized, single-axis control loop. For both pitch and yaw, modes 1 and 4 appear to dominate in the δ matrix, so that Θ_y and Θ_x could be approximated by equations of the form

$$\frac{\Theta_y(s)}{T_y(s)} = \left[I_{yy} s^2 - s^4 \frac{\delta_y^1 \delta_y^1}{(s^2 + 2\zeta_1\sigma_1 s + \sigma_1^2)} - s^4 \frac{\delta_y^4 \delta_y^4}{(s^2 + 2\zeta_4\sigma_4 s + \sigma_4^2)} \right]^{-1}$$

Table 2. TOPS hybrid-coordinate structural model data

Mode i	σ_i, Hz	$\Phi^T M \Sigma_{EO}$ (kg-m)			δ(kg-m^2)		
		x	y	z	x	y	z
1	0.74	0.2839 E-3	0.3557 E-3	0.1820 E01	-0.9479 E 1	-0.1559 E02	0.5230 E-2
2	0.75	0.1392 E01	0.1565 E01	-0.6839 E-3	-0.5334 E00	0.4858 E00	0.1802 E02
3	0.76	0.1319 E01	-0.1610 E01	-0.4712 E-4	0.5523 E00	0.4553 EQ0	0.1700 E02
4	0.76	-0.1766 E-3	-0.2151 E-3	0.2348 E01	-0.1216 E02	0.1172 E02	-0.1953 E-3
5	1.16	0.1235 E00	0.5553 E-2	0.6532 E-2	-0.2891 E-1	0.1992 E-1	0.6242 E01
6	3.85	-0.1216 E02	-0.13365 E00	-0.6915 E-2	0.2269 E00	0.8294 E00	-0.3575 E02
7	5.02	0.1782 E01	0.1965 E00	0.1079 E00	-0.8941 E00	0.5455 E01	0.1501 E01
8	5.66	-0.2009 E-1	-0.1075 E-1	-0.8343 E00	0.1163 E01	0.2636 E01	-0.9897 E-1
9	5.66	0.9229 E00	0.7903 E00	-0.3320 E-1	-0.1688 E00	0.3133 E00	0.3625 E01
10	5.69	-0.7921 E-1	0.4353 E-1	0.1075 E01	-0.1492 E01	0.2003 E01	-0.2894 E00

$$I = \begin{bmatrix} 1544.9 & -2.29 & -2.76 \\ -2.29 & 471.9 & -34.9 \\ -2.76 & -34.9 & 1714.4 \end{bmatrix} \quad \text{kg - m}^2 \text{ , } \mathcal{M} = 562.6 \text{ kg}$$

(The equation for $\theta_x(s)/T_x(s)$ is identical in form).

With the substitutions I_{xx}, I_{yy}, δ_y^1, δ_x^1, δ_y^4, δ_x^4 =(1544.9, 471.9, -15.6, -9.479,11.722, and - 12.16 Kg-M ^{2}), respectively, and σ_1, σ_4 = 4.65 and 4.76 rad/sec, respectively, and ζ_1, ζ_4 = 0.005, the resulting transfer functions for yaw and pitch are

$$\frac{\theta_y(s)}{T_y(s)} = \frac{(s^2 + 0.0465s + 21.62)(s^2 + 0.0476s + 22.8)}{1139s^2[0.405s^4 + 0.066s^3 + 31.1s^2 + 2.09s + 493]}$$

$$\frac{\theta_x(s)}{T_x(s)} = \frac{(s^2 + 0.0465s + 21.62)(s^2 + 0.0476s + 22.8)}{1139s^2[0.887s^4 + 0.089s^3 + 41.9s^2 + 2.09s + 493]}$$

The open-loop poles and zeros of the linearized, single-axis autopilot system of Figure 7 may now be plotted as shown in Figures 9 and 10. The dashed lines on Figures 9 and 10 indicate the closed-loop root locations under the ideal, totally rigid spacecraft condition where the control parameters are nominally specified as: τ_G = 1.77 sec, τ_F = 0.111 sec, ζ_G = 0.35, K_P = 2.2, ω_G = 88.0 rad/sec, ζ_s = 3.47, τ_P = 20.0 sec, and ω_s = 138.2 rad/sec; gimbal servo poles: -938.66, -20.35; gyro poles: -30.8 ±82.4 i; autopilot poles: -9.12, +0.059; gyro zero: -0.565; and path guidance zero: -0.05.

Loop gain (DC or Bode gain) at the point of marginal stability is 10.0. On the other hand, in Figure 9 the yaw axis loop with approximated flexible spacecraft dynamics shows a drastically changed root locus with a critical gain reduced to 2.9. While the pitch-axis root locus for the

flexible case also departs significantly from the rigid case, critical gain reduction is only to 8.5. The fact that the total pitch axis moment of inertia is about 3.3 times as great as yaw's obviously was responsible for the difference in location of the flexible appendage pole-zero contributions to each axis and the effect on critical loop gain values.

An examination of the rigid-body autopilot system reveals closed-loop bandwidths of about 0.3 and 0.8 Hz corresponding to DC loop gains of 1.0 (0 dB) and 3.16 (10 dB), respectively. It is clear that the first four appendage modes have already entered the control bandwidth at the latter gain level and, in the case of yaw, caused instability.

One might expect that, if additional modes are used in the initial single-axis root locus analyses, critical gain values would decrease even more. Further, the fact that interaxis coupling might require even more substantial loop gain reductions to maintain stability suggests an eigenvalue analysis of the complete system. The TOPS autopilot may be arranged into state variable form to give a 30 x 30 system state matrix including pitch, yaw, and roll angles, five flexible appendage modes, and the various control dynamics. Figure 11 shows that when the detailed, coupled case is considered, yaw loop stability deteriorates further and essentially controls the stability of the entire system.

A digital simulation was programmed and included nonlinearities due to (1) gimbal servo drive amplifier saturation, (2) the saturation characteristic built into the compensation block to prevent reaching mechanical gimbal stops, and (3) the roll axis bang-bang control loop. (It did not include gimbal actuator stiction.) The level of detail was

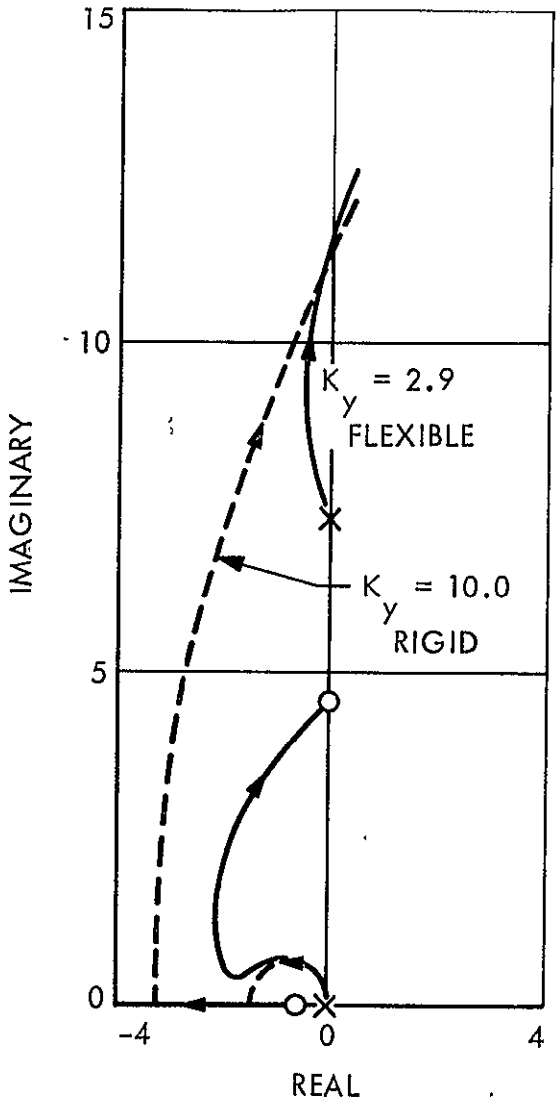

RIGID EFFECTS

7 OPEN-LOOP POLES

REAL	IMAG	ORDER
0.059	0.0	1
-9.12	0.0	1
-20.35	0.0	1
-938.7	0.0	1
-30.8	82.43	1
-30.8	-82.43	1
0.0	0.0	2

2 OPEN-LOOP ZERO(S)

REAL	IMAG	ORDER
-0.05	0.0	1
-0.565	0.0	1

FLEXIBILITY EFFECTS

4 OPEN-LOOP POLES

REAL	IMAG	ORDER
-0.0579	-7.37	1
-0.0579	7.37	1
-0.0237	-4.73	1
-0.0237	4.73	1

4 OPEN-LOOP ZERO(S)

REAL	IMAG	ORDER
-0.0239	-4.77	1
-0.0239	4.77	1
-0.0232	-4.64	1
-0.0232	4.64	1

Figure 9. TOPS autopilot yaw axis root locus

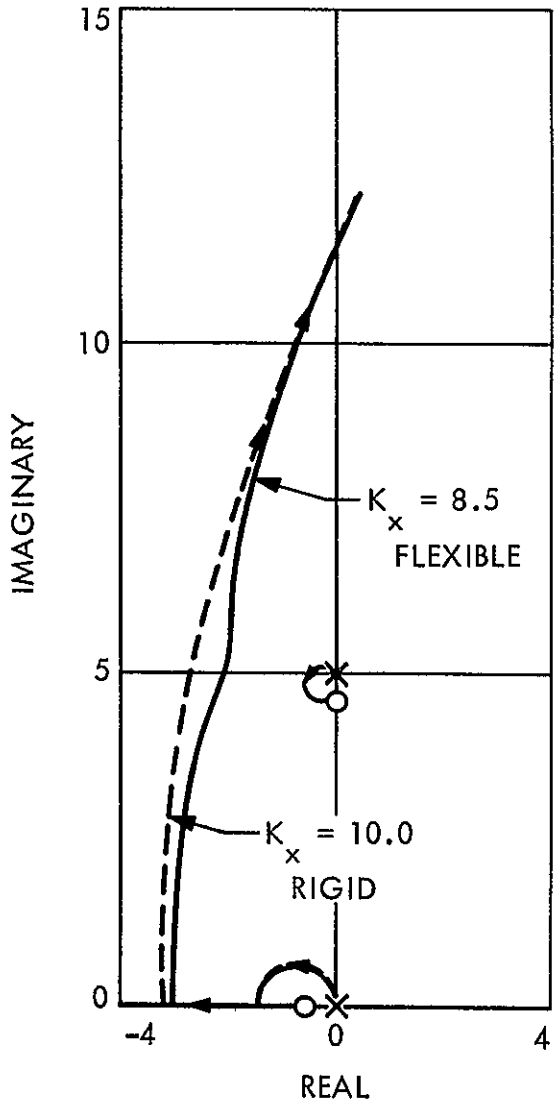

RIGID EFFECTS

7 OPEN-LOOP POLES

REAL	IMAG	ORDER
0.059	0.0	1
-9.12	0.0	1
-20.35	0.0	1
-938.7	0.0	1
-30.8	82.43	1
-30.8	-82.43	1
0.0	0.0	2

2 OPEN-LOOP ZERO(S)

REAL	IMAG	ORDER
-0.05	0.0	1
-0.565	0.0	1

FLEXIBILITY EFFECTS

4 OPEN-LOOP POLES

REAL	IMAG	ORDER
-0.0267	-5.03	1
-0.0267	5.03	1
-0.0235	-4.68	1
-0.0235	4.68	1

4 OPEN-LOOP ZERO(S)

REAL	IMAG	ORDER
-0.0239	-4.77	1
-0.0239	4.77	1
-0.0232	-4.64	1
-0.0232	4.64	1

Figure 10. TOPS autopilot pitch axis root locus

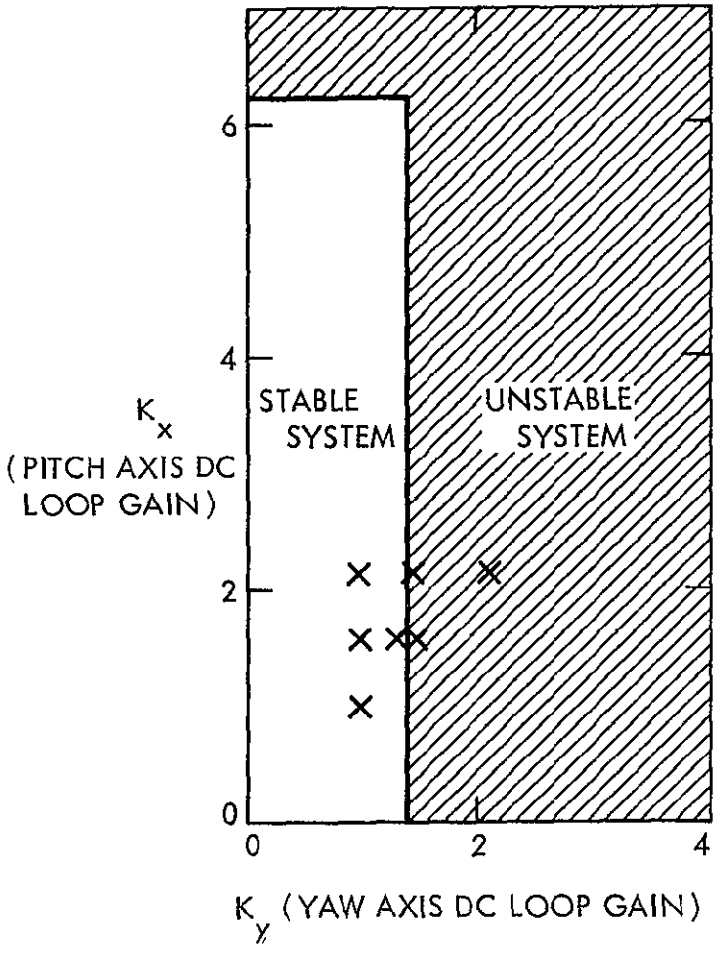

Figure 11. Stability diagram

such as to include effects of gimbal mounting errors and center-of-mass displacements due to appendage deformations, and the hybrid coordinate formulation represented by Eqs. (224) and (216) of Reference 1 was implemented in detail. Yaw-axis response is shown for three cases in Figures 12 and 13 to illustrate the computer simulation results. In each case, the autopilot controller and spacecraft are responding to the engine turn-on transient (445 N) under the conditions of an initial pitch axis center-of-mass offset of (.05 cm) Five flexible modes are used in each case in Figure 13; for gains of 2.2 the flexible vehicle proves to be unstable (Figure 13a) as the eigenvalue analysis predicted. Reduction of $K_{x,y}$ to 1.0 results in a stable response (Figure 13b), which also agrees with eigenvalue predictions.

APPENDIX C -- THE ATTITUDE CONTROL OF A FLEXIBLE SOLAR ELECTRIC SPACECRAFT:

Introduction:

During the cruise-low thrust phase of the mission of the solar electric spacecraft illustrated in Figure 14, one means of providing three axis attitude control is the combination of translation and gimballing of the electric propulsion engines. This concept will be analyzed in the sequel. Inclusion of the elastic effects of the flexible solar arrays was accomplished by utilization of the hybrid coordinate procedures described in Reference 1.

Figure 14 shows the spacecraft to be analyzed. It is composed of a rigid central body B_1 to which are attached two flexible roll out solar arrays A, and an engine cluster E. Unit vectors $\underline{b}_1$, $\underline{b}_2$ and $\underline{b}_3$ are fixed in B_1. Figure 15 shows E in more detail. The engine cluster consists

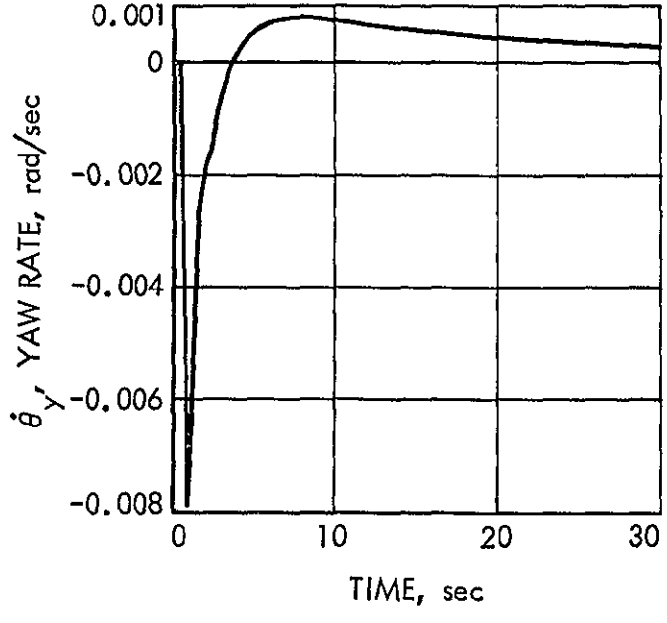

Figure 12. Yaw axis response, rigid vehicle, $K_x = K_y = 2.2$

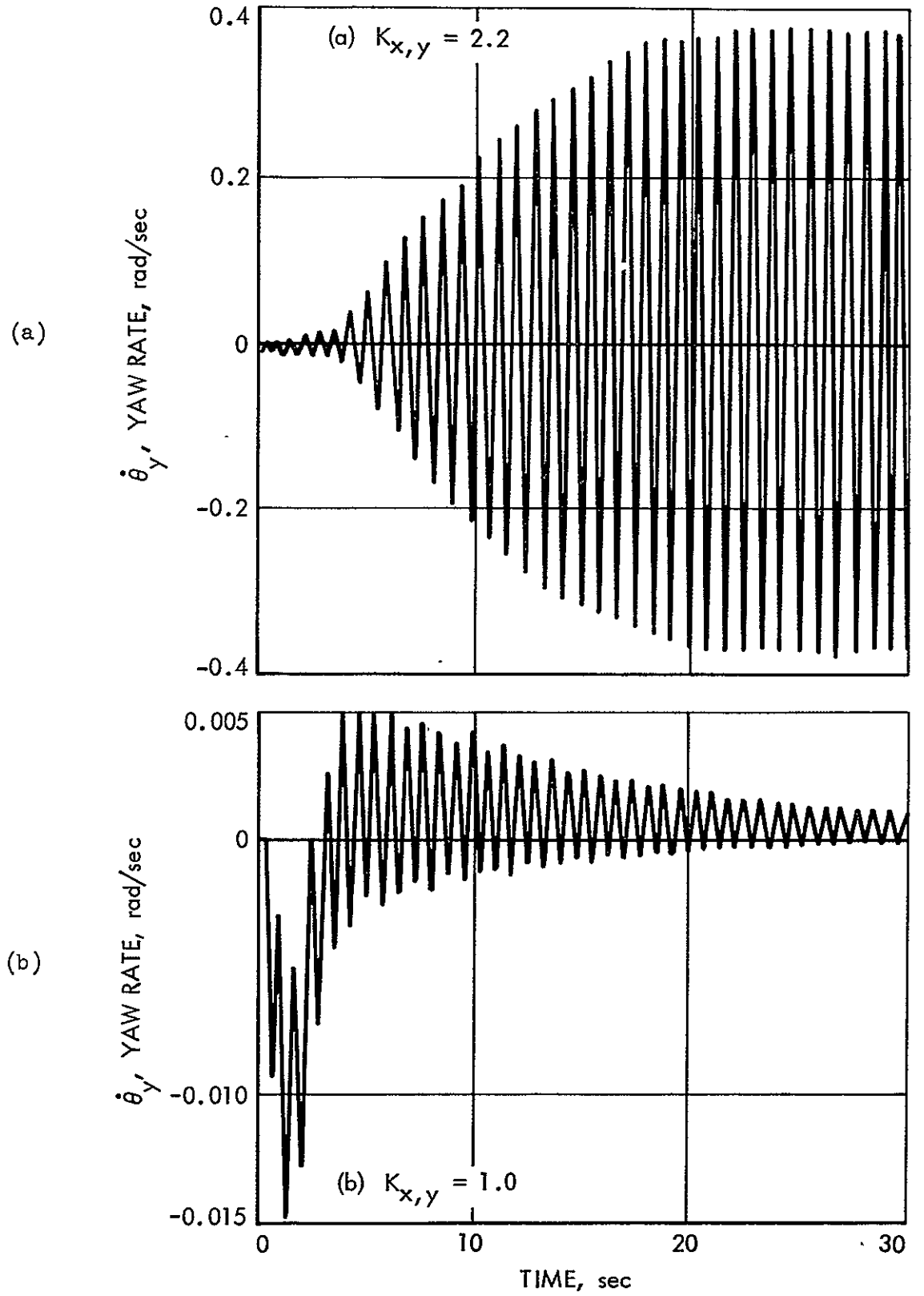

Figure 13. Yaw axis response, flexible vehicle

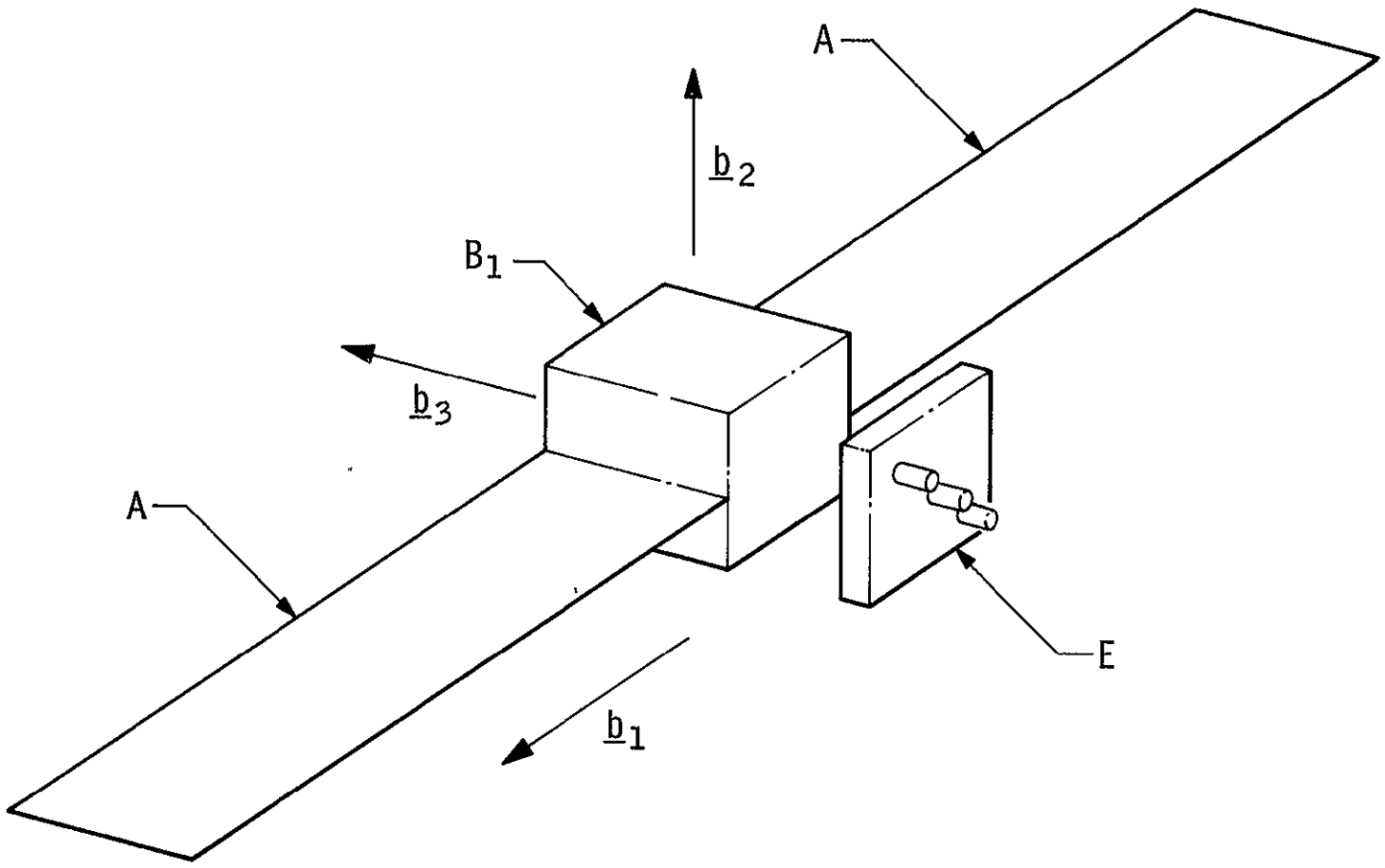

Figure 14. Solar Electric Spacecraft

Figure 15. Engine Cluster

of a large plate to which are attached three electric propulsion engines and a unit containing translating mechanisms. Two of the engines, B_3 and B_4, can rotate about the diagonal passing through the $\underline{b}_1$ - $\underline{b}_2$ quadrant. The plate and the remaining engine are denoted B_2. E can translate parallel to the $\underline{b}_1$ direction and B_2 can translate parallel to the $\underline{b}_2$ direction. Figure 15b shows the cluster in an arbitrary configuration. Point O is the mass center of the entire spacecraft for the case of no engine translation or gimballing.

During the cruise low-thrust phase, when E translates parallel to $\underline{b}_1$, a control moment parallel to $\underline{b}_2$ is exerted on the spacecraft. Translation of B_2 parallel to $\underline{b}_2$, will produce a moment parallel to $\underline{b}_1$. Third axis control is provided by the gimballing of engines B_3 and B_4. This generates a moment parallel to $\underline{b}_3$.

Figure 16 shows E in even greater detail. In addition to B_2, B_3, and B_4, bodies B_5, B_6 and B_7 are shown. These are associated with the mechanisms which translate E. B_5 and B_6 are drums with axes fixed in the translating mechanism unit. Two tapes are wrapped about B_5. Each has one end attached to B_5. The remaining ends are fixed in B_1. Hence, when B_5 rotates, one tape winds up on the drum while the other unwinds. Consequently, E translates along the shafts parallel to $\underline{b}_1$. A second assembly consisting of B_6 and two tapes accounts for translation parallel to $\underline{b}_2$ except that the tapes are attached to B_2, instead of B_1. B_7 is the unit containing B_5, B_6 and the motors which drive them.

Differential equations of motion for the entire vehicle, the appendages A, and the rigid bodies B_2, ..., B_7 will be stated.

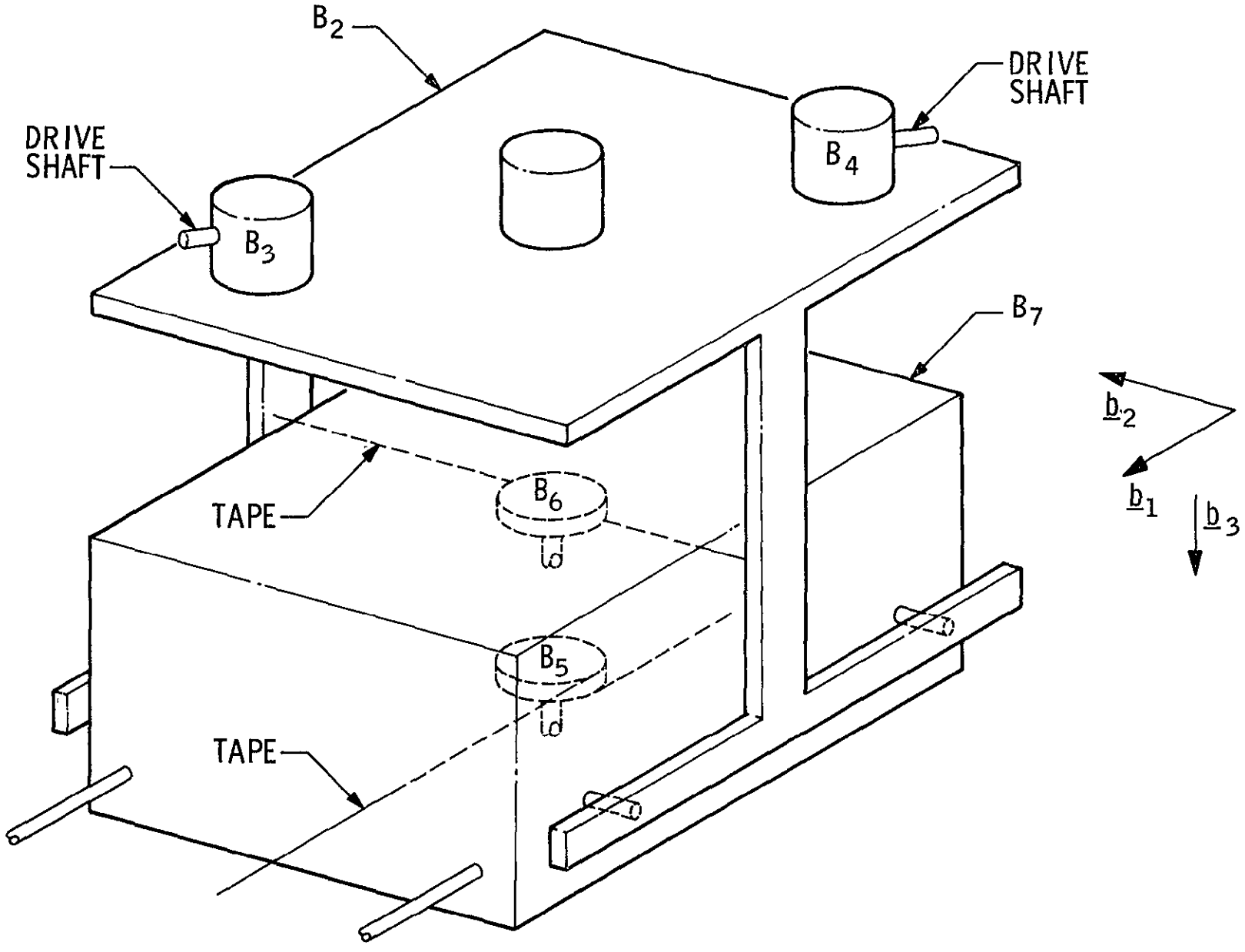

Figure 16 Translator

Vehicle Equations:

For the assembly of bodies shown in Figures 14 and 16 the vehicle equation is, from Reference 1,

$$\underline{T} = \underline{\underline{I}} \cdot \dot{\underline{\omega}} + \underline{\omega} \times \underline{\underline{I}} \cdot \underline{\omega} + \mathring{\underline{\underline{I}}} \cdot \underline{\omega} + \left[\mathring{\underline{c}}^{\circ\circ} + 2\,\underline{\omega} \times \mathring{\underline{c}}^{\circ}\right.$$

$$\left. + \underline{\omega} \times (\underline{\omega} \times \underline{c}) + \dot{\underline{\omega}} \times \underline{c}\right] \times \underline{c} + \frac{\mathcal{I}_d}{dt} \int \underline{p} \times \mathring{\underline{p}} \, dm \qquad (1)$$

where

$\underline{T}$ - torque applied to vehicle.

$\underline{\underline{I}}$ - vehicle inertia dyadic.

$\underline{\omega}$ - angular velocity of B_1 in inertial space.

- total vehicle mass.

$\underline{c}$ - mass center shift vector.

$\mathcal{I}$ - an inertial reference frame.

$\underline{p}$ - position vector of a generic point of the vehicle with respect to O.

dm - differential element of mass.

$(\dot{})$ - derivative of a vector or dyadic in b, or the derivative of a scalar.

$(\mathring{})$ - derivative of a vector or dyadic in b, a reference frame in which the unit vectors $\underline{b}_1$, $\underline{b}_2$, $\underline{b}_3$ are fixed.

In more detail, the matrix form of the vehicle equation is

$$T = \left[I^* + \sum_{i=2}^{7} (-M_i \tilde{p}^{i*} \tilde{p}^{i*} + T^{1T} I^i T^i)\right] \dot{\omega}$$

$$+ \tilde{\omega}[I^{*} + \sum_{i=2}^{7} (-M_i \tilde{p}^{i*} \tilde{p}^{i*} + T^{iT} I^{i} T^{i})]\omega$$

$$+ \{2M(\Sigma_{EO} R + \rho)^{T} q - Rq^{T} M \Sigma_{EO} - \Sigma_{EO}^{T} MqR^{T} - \rho^{\dagger} (Mq)^{\dagger T}$$

$$- (Mq)^{\dagger} \rho^{\dagger} + \Sigma_{EO}^{T} (\tilde{q}M - \tilde{Mq}) \Sigma_{OE}\}\dot{\omega}$$

$$+ \{- \sum_{i=2}^{7} M_i [\tilde{\dot{p}}^{i*} \tilde{p}^{i*} + (\tilde{\dot{p}}^{i*} \tilde{p}^{i*})^{T}]$$

$$+ \sum_{i=2}^{7} (\dot{T}^{iT} I^{i} T^{i} + T^{iT} I^{i} \dot{T}^{i})\} \omega + m(\ddot{c} + 2\tilde{\omega}\dot{c} + \tilde{\omega}\tilde{\omega}c + \dot{\tilde{\omega}}c)\tilde{c}$$

$$+ \sum_{i=2}^{7} \{M_i (\tilde{\dot{p}}^{i*} \dot{p}^{i*} + \tilde{\omega} \tilde{p}^{i*} \dot{p}^{i*})$$

$$+ (\dot{T}^{iT} I^{i} T^{i} + T^{iT} I^{i} \dot{T}^{i} + \tilde{\omega} T^{iT} I^{i} T^{i}) \omega^{i} + T^{iT} I^{i} T^{i} \dot{\omega}^{i}\}$$

$$+ (\tilde{\omega}R)\tilde{} \Sigma_{EO}^{T} M\dot{q} + \tilde{R} \Sigma_{EO}^{T} M\dot{q} + \tilde{R} \tilde{\omega} \Sigma_{EO}^{T} M\dot{q} + \Sigma_{EO}^{T} \tilde{\rho} M\dot{q}$$

$$+ \Sigma_{OE}^{T} M\dot{q} + \tilde{\omega} \Sigma_{OE}^{T} M\dot{q} - \tilde{\omega} \Sigma_{OE}^{T} \tilde{\rho} M + \Sigma_{OE}^{T} M(\Sigma_{OE}\omega)\tilde{} \dot{q}$$

$$- \Sigma_{EO}^{T}(\tilde{\rho}\ \Sigma_{EO}\omega)\tilde{M}\dot{q} + \Sigma_{OE}^{T}\dot{\tilde{q}}M\ \Sigma_{OE}\omega + \tilde{\omega}\ \Sigma_{OE}^{T}\tilde{q}M\ \Sigma_{OE}\omega$$

$$- \tilde{\omega}\ \Sigma_{OE}^{T}M\tilde{q}\ \Sigma_{OE}\omega + \tilde{\omega}\{2[M(\Sigma_{EO}R + \rho)]^{T}q$$

$$- Rq^{T}M\ \Sigma_{EO} - \Sigma_{EO}^{T}MqR^{T} - \rho^{\dagger}(Mq)^{\dagger T} - (Mq)^{\dagger}\rho^{\dagger T}\}\omega$$

$$+ \{2[M(\Sigma_{EO}R + \rho)]^{T}\dot{q} - R\dot{q}^{T}M\ \Sigma_{EO} - \Sigma_{EO}^{T}M\dot{q}R^{T}$$

$$- \rho^{\dagger}(M\dot{q})^{\dagger T} - (M\dot{q})^{\dagger}\ \rho^{\dagger T}\}\omega \qquad (2)$$

where

T - applied torque matrix.

I^{*} - inertia matrix for B_1 and A in the undeformed state.

M_i - mass of B_i.

p^{*i} - position vector of P_i^{*}, the mass center of B_i, with respect to O.

T^{i} - transformation matrix from principal axes of B_i to principal axes of B_1.

I^{i} - inertia matrix for B_i.

ω - angular velocity of B_1 in $\mathcal{I}$.

M - the nxn mass matrix for A where n is the number of sub-bodies comprising the model which approximates A.

R - position vector of a point Q on the appendage - B_1 interface with respect to O.

ρ - position vector of the mass center of a sub-body of A with respect to Q.

q - deformation coordinate vector for A.

Σ_{EO} - the matrix $[EOEO...EO]^T$ of size 6nx3 where E is the 3x3 identity matrix.

Σ_{OE} - the matrix $[OE...OE]^T$.

c - mass center shift vector.

$\sim$ - when applied to a 3 x 1 vector, $v = [v_1 v_2 v_3]^T$, $\tilde{v}$ means

$$\begin{bmatrix} 0 & -v_3 & v_2 \\ v_3 & 0 & -v_1 \\ -v_2 & v_1 & 0 \end{bmatrix}$$

when applied to the 3 x 6n matrix $v = [v^1 0 v^2 0 ... v^n 0]$, where v^i is a 3 x 1 vector, $\tilde{v}$ means

$$\tilde{v} = \begin{bmatrix} \tilde{v}^1 & & & & & & \\ & 0 & & & & & \\ & & \tilde{v}^2 & & & & \\ & & & 0 & & & \\ & & & & \cdot & & \\ & & & & & \cdot & \\ & & & & & & \tilde{v}^n \\ & & & & & & & 0 \end{bmatrix}$$

$( )^T$ - the transpose of a matrix.

$( )^\dagger$ - if $v = [v^1 0 v^2 0 \ldots v^n 0]^T$, then

$$v^\dagger = [v^1 0 v^2 0 \ldots v^n 0].$$

An expression for c is

$$c = -\frac{1}{m}\left(\Sigma_{E0}^T M q + \sum_{i=2}^{7} M_i \delta^{\dot{1}}\right) \tag{3}$$

where $\delta^{\dot{i}}$ is the displacement vector for B_i.

If engines B_2, B_3, and B_4 are thrusting at the constant magnitude F, and there are no disturbance torques exerted on the vehicle other than from the thrust, then

$$\begin{aligned} T = {} & \{p^{2*0} + \frac{1}{m}[(m - m)r^1 + (m - \bar{m})r^2 \\ & - \Sigma_{E0}^T M q]\}^{\sim} \begin{bmatrix} 0 \\ 0 \\ F \end{bmatrix} + \{p^{3*0} + \frac{1}{m}[m - m)r^1 \\ & + (m - \bar{m})r^2 - \Sigma_{E0}^T M q]\}^{\sim} \frac{1}{\sqrt{2}} \begin{bmatrix} Fs_3 \\ -Fs_3 \\ \sqrt{2}Fc_4 \end{bmatrix} \\ & + \{p^{4*0} + \frac{1}{m}[(m - m)r^1 + (m - \bar{m})r^2 \\ & - \Sigma_{E0}^T M q]\}^{\sim} \frac{1}{\sqrt{2}} \begin{bmatrix} Fs_4 \\ -Fs_4 \\ \sqrt{2}Fc_4 \end{bmatrix} \end{aligned} \tag{4}$$

where

p^{i*0} - position vector of P_i^*, the mass center of B_i, with respect to 0 for the nominal state.

$m = \sum_{i=2}^{7} M_i$.

$\bar{m} = M_2 + M_3 + M_4$.

$r^1 = [-r\alpha_5 \; 0 \; 0]^T$.

$r^2 = [0 \; -r\alpha_8 \; 0]^T$.

α_i - the angle through which B_i turns relative to B_1.

s_i - $\sin \alpha_i$, i=2,...,7.

c_1 - $\cos \alpha_1$, i=2,...,7.

r - the radius of B_5 or B_6.

Appendage Equations:

The appendage equation is taken directly from Eqs. (94) and (95) of Reference 1.

$$M(E - \Sigma_{EO}\Sigma_{EO}^T M/m)\ddot{q} + \{2M[(\Sigma_{EO}\omega)^{\sim} - \Sigma_{EO}\tilde{\omega}\Sigma_{EO}^T m/m]$$

$$+ M(\Sigma_{OE}\omega)^{\sim} + (\Sigma_{OE}\omega)^{\sim} M - [M\Sigma_{OE}\omega]^{\sim} + D'\}\dot{q}$$

$$+ \{M(\Sigma_{OE}\dot{\omega})^{\sim} - (M\Sigma_{OE}\dot{\omega})^{\sim} - (\Sigma_{OE}\omega)^{\sim}(M\Sigma_{OE}\omega)^{\sim}$$

$$+ (\Sigma_{OE}\omega)^{\sim} M(\Sigma_{OE}\omega)^{\sim} + M[\Sigma_{EO}\dot{\omega})^{\sim} - \Sigma_{EO}\tilde{\dot{\omega}}\Sigma_{EO}^T M/m]$$

$$+ M[(\Sigma_{EO}\omega)^{\sim}(\Sigma_{EO}\omega)^{\sim} - \Sigma_{EO}\tilde{\omega}\tilde{\omega}\Sigma_{EO}^{T}M/m\ ] + K']q$$

$$= - M\Sigma_{OE}\dot{\omega} - (\Sigma_{OE}\omega)^{\sim}M(\Sigma_{OE}\omega) - M\{\Sigma_{EO}[\ddot{\varrho x}$$

$$- (\tilde{R} + \tilde{e})\dot{\omega} + \ddot{e} - 2\dot{\tilde{e}}\,\omega + \tilde{\omega}\,\tilde{\omega}(R + e)]$$

$$- \tilde{\rho}\,\Sigma_{EO}\dot{\omega} - (\Sigma_{EO}\omega)^{\sim}(\Sigma_{EO}\omega)^{\sim}\rho\} + \lambda \qquad (5)$$

where the new symbols mean

D' - damping matrix.

K' - stiffness matrix.

$\ddot{\varrho x}$ - acceleration of O_T in $\mathcal{I}$ expressed in terms of $\{b\} = [\underline{b}_1\underline{b}_2\underline{b}_3]^T$

λ - forces and torques, other than from structural interactions which are applied to the sub-bodies.

e - the mass center shift vector associated with B_i, i=2,...,7. This is the second term in the expression in Eq. (3) for c.

Rigid Body B_i (i=2,...7) Equations:

The units $B_2 \ldots B_7$ constitute the translator. Equations for the coordinates associated with its translation and the gimballing of B_3 and B_4 are required. It appears as if use of Lagrange's equations provides the most convenient means of determining these equations. The standard form for these equations is

$$\frac{d}{dt}\left(\frac{\partial L}{\partial \dot{y}_i}\right) - \frac{\partial L}{\partial y_i} = Q_i \tag{6}$$

where L is the Lagrangian for the spacecraft, y_i, is a generalized coordinate, and Q_i is the generalized force corresponding to y_i. L is

$$L = K - P \tag{7}$$

where K and P are the kinetic and potential energies, respectively, of the spacecraft. Equations (2) and (3) govern the behavior of ω and q. In using Eq. (6), then, we will restrict attention to coordinates other than ω and q.

The following assumptions are made for the translator assembly (refer to Figures 15 and 16):

1. For the translator assemblies, shafts connecting either B_5 or B_6 to the motors driving them have non-infinite stiffness.
2. Non-infinite stiffness is associated only with the drive shafts which cause B_3 and B_4 to gimbal.
3. All drive shaft bearings are not smooth.
4. The mass centers of B_3 and B_4 lie on their gimbal axes.
5. The translation shaft bearings are not smooth.

The nonlinear equations of motion for α_5 and α_6 are

$$I_1^3\left[\ddot{\alpha}_3 + \frac{1}{\sqrt{2}}(\dot{\omega}_1 + \dot{\omega}_2)\right] - (I_3^3 - I_1^3)\left[\frac{1}{\sqrt{2}} c_3(\omega_1 - \omega_2)\right.$$

$$\left. - s_3\omega_3\right]\left[\frac{1}{\sqrt{2}} s_3(\omega_1 - \omega_2) + c_3\omega_3\right] - k_3(\alpha_{G1} - \alpha_3) = -d_3\alpha_3 \tag{8}$$

$$I_1^3[\ddot{\alpha}_4 + \frac{1}{\sqrt{2}}(\dot{\omega}_1 + \dot{\omega}_2)] - (I_3^3 - I_1^3)[\frac{1}{\sqrt{2}} c_4(\omega_1 - \omega_2)$$

$$- s_4\omega_3][\frac{1}{\sqrt{2}} s_4(\omega_1 - \omega_2) + c_4\omega_3] - k_4(\alpha_{G2} - \alpha_4) = -d_4\alpha_4 \quad (9)$$

$$(mr^2 + I_3^5)\ddot{\alpha}_5 - mrE^{1T}\ddot{\theta X} - \mu r\dot{\omega}_2 + I_3^5\dot{\omega}_3$$

$$- \bar{m}r^2(\dot{\omega}_3\alpha_6 + \omega_3\dot{\alpha}_6) \qquad - (\omega_2^2 + \omega_3^2)mr^2\alpha_5$$

$$+ \bar{m}r^2\omega_1\omega_2\alpha_6 - \mu r\omega_3\omega_1 - \bar{m}r^2\omega_3\dot{\alpha}_6$$

$$- mr(E^{3T}\omega_2 - E^{2T}\omega_3)\theta\dot{x} - k_2(\alpha_{T2} - \alpha_5)$$

$$+ \frac{m^3}{\mathcal{M}^2} r^2\ddot{\alpha}_5 + \frac{m^2\bar{m}}{\mathcal{M}^2}r^2\ddot{\alpha}_6 + \frac{m^2}{\mathcal{M}}rE^{1T}(\dot{\theta}\dot{x} + \theta\ddot{x}) - mr\ddot{c}_1^A$$

$$- 2\frac{m^2}{\mathcal{M}} r^2\ddot{\alpha}_5 + \frac{mr\mu}{\mathcal{M}}\dot{\omega}_2 + \frac{m}{\mathcal{M}} r^2\bar{m}(\dot{\omega}_3\alpha_6 + \omega_3\dot{\alpha}_6) + \frac{m^2r}{\mathcal{M}}\ddot{c}_1^A$$

$$+ mr\omega_3\dot{c}_2^A - mr\omega_2\dot{c}_3^A + (\bar{m}\, m/\mathcal{M})r^2\omega_3\dot{\alpha}_6$$

$$- \mu r(\dot{\omega}_2 c_3^A + \omega_2\dot{c}_3^A - \dot{\omega}_3 c_2^A - \omega_3\dot{c}_2^A) + \frac{m\bar{m}}{\mathcal{M}}r^2(\dot{\alpha}_6\omega_3 + \alpha_6\dot{\omega}_3)$$

$$+ \frac{m^2r}{\mathcal{M}}(\dot{\omega}_2 c_3^A + \omega_2\dot{c}_3^A - \dot{\omega}_3^A c_2^A\, \omega_3\dot{c}_2^A)$$

$$+ \frac{m^2r}{\mathcal{M}}(- \omega_3 E^{2T}\theta\dot{x} + \omega_2 E^{3T}\theta\dot{x}) + \frac{\bar{m}\, m}{\mathcal{M}}r^2\alpha_6\omega_3$$

$$+ mr\omega_3(\omega_3 c_1^A - \omega_1 c_3^A) - mr\omega_2(\omega_1 c_2^A - \omega_2 c_1^A)$$

$$+ \frac{2m^2}{\mathcal{M}} r^2 \alpha_5 \omega_3^2 + \frac{m\mu r}{\mathcal{M}} \omega_1 \omega_3 - \frac{m\bar{m}}{\mathcal{M}} r^2 \alpha_6 \omega_1 \omega_2 + \frac{2m^2}{\mathcal{M}} r^2 \alpha_5 \omega_2^2$$

$$- \frac{m\bar{m}}{\mathcal{M}} r^2 \omega_2 \omega_1 - \frac{m^2}{\mathcal{M}} r \dot{c}_2^A \omega_3 + \frac{m^2}{\mathcal{M}} r \dot{c}_3^A \omega_2 - \frac{m^2 r}{\mathcal{M}} (\omega_3 c_1^A - \omega_1 c_3^A) \omega_3$$

$$+ \frac{m^2 r}{\mathcal{M}} (\omega_1 c_2^A - \omega_2 c_1^A) \omega_2 - \frac{2m^3}{\mathcal{M}^2} r^2 \alpha_5 \omega_3 - \frac{2m^3}{\mathcal{M}^2} r^2 \alpha_5 \omega_2^2$$

$$+ 2\frac{m^2\bar{m}}{\mathcal{M}} \alpha_6 \omega_1 \omega_2 = - \frac{rF}{\sqrt{2}} (s_3 + s_4) - d_2 r^2 \dot{\alpha}_5 \qquad (10)$$

$$(\bar{m}r^2 + I_3^6) \ddot{\alpha}_6 - \bar{m}rE^{2T} \ddot{\theta x} + \bar{\mu} r \dot{v}_1 + I_3^6 \dot{\omega}_3$$

$$+ \bar{m}r^2 (\dot{\omega}_3 \alpha_5 + \omega_3 \dot{\alpha}_5) - (\omega_1^2 + \omega_3^2) \bar{m}r^2 \alpha_6 + \bar{m}r^2 \omega_1 \omega_2 \alpha_5$$

$$- \bar{\mu} r \omega_2 \omega_3 - \bar{m}r(E^{1T} \omega_3 - E^{3T} \omega_1) \dot{\theta x} + \bar{m}r^2 \omega_3 \dot{\alpha}_5$$

$$- k_1 (\alpha_{T1} - \alpha_6) + \frac{m\bar{m}^2}{\mathcal{M}^2} r^2 \ddot{\alpha}_6 + \frac{m^2\bar{m}}{\mathcal{M}^2} r^2 \ddot{\alpha}_5$$

$$+ \frac{m\bar{m}}{\mathcal{M}} rE^{2T} (\dot{\theta x} + \theta \ddot{x}) - \bar{m}r \ddot{c}_2^A - \frac{2\bar{m}^2}{\mathcal{M}} r^2 \ddot{\alpha}_6 - \frac{\bar{m}r\mu}{\mathcal{M}} \dot{\omega}_1$$

$$- \frac{\bar{m}m}{\mathcal{M}} r^2 (\dot{\omega}_3 \dot{\alpha}_5 + \omega_3 \ddot{\alpha}_5) + \frac{m\bar{m}}{\mathcal{M}} r \ddot{c}_2^A - \bar{m}r\omega_3 \dot{c}_1^A + \bar{m}r\omega_1 \dot{c}_3^A$$

$$- \frac{\bar{m}m}{\mathcal{M}} r^2 \omega_3 \dot{\alpha}_5 - \bar{m}r(\dot{\omega}_3 c_1^A + \omega_3 \dot{c}_1^A + \dot{\omega}_1 c_3^A - \omega_1 \dot{c}_3^A)$$

$$- \frac{\bar{m}m}{\mathcal{M}} r^2 (\dot{\alpha}_5 \omega_3 + \alpha_5 \dot{\omega}_3) + \frac{m\bar{m}}{\mathcal{M}} r (\dot{\omega}_3 c_1^A + \omega_3 \dot{c}_1^A - \dot{\omega}_1 c_3^A$$

$$- \omega_1 \dot{c}_3^A + \frac{m\,\bar{m}r}{m}(\omega_3 E^{1T}\Theta\dot{x} - \omega_1 E^{3T}\Theta\dot{x})$$

$$- \frac{m\,\bar{m}}{m}\dot{\alpha}_5\omega_3 - \bar{m}r\omega_3(\omega_2 c_3^A - \omega_3 c_2^A) + \bar{m}r\omega_1(\omega_1 c_2^A - \omega_2 c_1^A)$$

$$- \frac{m\,\bar{m}}{m}r^2\alpha_5\omega_1\omega_2 + \frac{\bar{m}_L r}{m}\omega_2\omega_3 + \frac{2\bar{m}^2}{m}r^2\alpha_6\omega_3^2 + \frac{\bar{m}^2}{m}r^2\omega_1^2$$

$$+ \frac{m\,\bar{m}}{m}r\dot{c}_1^A\omega_3 - \frac{m\,\bar{m}}{m}r\dot{c}_3^A\omega_1 + \frac{m\,\bar{m}r}{m}(\omega_2 c_3^A - \omega_3 c_2^A)$$

$$- \frac{m\,\bar{m}r}{m}(\omega_1 c_2^A - \omega_2 c_1^A)\omega_1 - \frac{2m\,\bar{m}r^2}{m}\alpha_6\omega_3^2 - \frac{2m\,\bar{m}^2}{m}\alpha_6\omega_1^2$$

$$= - \frac{rF}{\sqrt{2}}(s_3 + s_4) - d_1 r^2\dot{\alpha}_6 \qquad (11)$$

where

I_j^i - moment of inertia of B_i for the axis parallel to $\underline{b}_j$

ω_i - $\underline{b}_i \cdot \underline{\omega}$, $i = 1,2,3$.

k_i - spring constant associated with the translating or gimbaling mechanisms.

d_i - damping constant associated with the translating or gimbaling mechanisms.

E^{1T}, E^{2T}, E^{3T} - [1 0 0], [0 1 0], [0 0 1].

c_i^A - measure number of mass center shift due to flexibility.

μ - $\Sigma M_i p_3^{i*}$, where p_3^{i*} is the $\underline{b}_3$ component of p^{i*0}, the value of p^{i*} for the nominal state.

T_i - torque applied to B_i.

α_{Gi} - gimbal drive shaft input angle.

α_{Ti} - translating drive shaft input angle.

Linearized Equations of Motion:

It can be shown by substitution that

$$\omega = \alpha_i = \lambda = \alpha_{G1} = \alpha_{G2} = \alpha_{T1} = \alpha_{T2} = 0$$

$$x = x_o, \ \theta = \theta_o \tag{12}$$

$$q = q_o = - K^{-1} M \Sigma_{EO} \theta_o \ddot{x}_o$$

is a solution to Eqs. (2), (5), (8)-(11). Determination of the linearized variational equations associated with this solution and introduction of the active control equations establishes the base for a stability analysis by means of root locus procedures or eigenvalue analyses.

The variational equations are obtained by substitution of

$$\omega = \omega'$$

$$\alpha^i = \alpha^{i\prime}$$

$$q = q_o + q' \tag{13}$$

$$\alpha_{Gi} = \alpha'_{Gi}, \ \alpha_{Ti} = \alpha'_{Ti}$$

$$x = x_o + x'$$

$$\theta = \theta_o + \theta'$$

into Eqs. (2), (5), (8)-(11) and linearizing in the primed variables. λ is set equal to zero.

The appendage equation takes the form

$$M'\ddot{q}' + D'\dot{q}' + K'q' = M(-\Sigma_{OE} + \Sigma_{EO}^{T}\tilde{R} + \tilde{r}\Sigma_{EO})\ddot{\theta}'$$

$$+ M\Sigma_{EO}\tilde{F}^{2}(\alpha'_{3} + \alpha'_{4}) + \frac{M}{m}\Sigma_{EO}\sum_{i=2}^{7} M_i\ddot{\delta}^{i},$$

where

$$M' = M(E - \Sigma_{EO}\Sigma_{EO}M/m)$$

In all of the following discussion, the primes will be omitted from the linearized system variables. If the modal coordinates η are defined by $q = \phi\eta$, where ϕ is the matrix of eigenvectors for

$$M'\ddot{q} + K'q = 0$$

and if $\bar{\phi}$ and $\bar{\eta}$ denote N x N truncated versions of ϕ and η where $N < n$, and if $\bar{\delta}$ and $\bar{\Delta}$ (hereafter referred to as the rigid-elastic coupling terms) are defined by

$$\bar{\delta} = -\bar{\phi}^{T}M'(\Sigma_{OE} - \Sigma_{EO}\tilde{R} - \tilde{r}\Sigma_{EO})$$

$$\bar{\Delta} = \bar{\phi}^{T}M\Sigma_{EO}$$

then the appendage equation becomes

$$E\ddot{\bar{\eta}} + 2\bar{\zeta}\,\bar{\sigma}\,\dot{\bar{\eta}} + \bar{\sigma}^{2}\bar{\eta} = \bar{\delta}\ddot{\theta} + \bar{\Delta}\tilde{F}^{2}(\alpha_3 + \alpha_4) + \frac{\bar{\Delta}}{m}(m\ddot{r}^{1} + \bar{m}\ddot{r}^{2})$$

where E is the N x N unit matrix, $\bar{\sigma}$ is the N x N diagonal matrix of eigenvalues or mode frequencies, $\bar{\zeta}$ is the N x N diagonal matrix of damping ratios, F^2 is the thrust vector for the center engine, and r^1 and r^2 are vectors describing the $\underline{b}^1$ and $\underline{b}^2$ migrations of the translator from its nominal position

$$r^1 = [-r\alpha_5,\ 0,\ 0]^T,\quad r^2 = [0,\ -r\alpha_6,\ 0]^T$$

It will be assumed that $\alpha_4 = -\alpha_3$. Then, the appendage equation becomes

$$E\ddot{\bar{\eta}} + 2\bar{\zeta}\,\bar{\sigma}\,\dot{\bar{\eta}} + \bar{\sigma}^2\bar{\eta} = \bar{\delta}\ddot{\vartheta} + \frac{\bar{\Delta}}{m}(m\ddot{r}^1 + \bar{m}\ddot{r}^2) \qquad (14)$$

The torque T exerted on the vehicle may be expressed as

$$T = \sum_{i=2}^{4} \tilde{s}^i F^i$$

where F^i is the thrust force supplied by B_i, i=2, 3, 4, and s^i is the position vector of the point of application of F^i with respect to the vehicle mass center. It can be shown that a more explicit non-linear expression for T is

$$T = \left[p^{2*0} + \frac{m - \bar{m}}{m} r^1 + \frac{m - \bar{m}}{m} r^2 - \frac{1}{m} r_{EO}^T M q\right]^{\sim} \begin{bmatrix} 0 \\ 0 \\ F \end{bmatrix}$$

$$+ \left[p^{3*0} + \frac{m - \bar{m}}{m} r^1 + \frac{m - \bar{m}}{m} r^2 - \frac{1}{m} r_{EO}^T M q\right]^{\sim} \frac{1}{\sqrt{2}} \begin{bmatrix} Fs_3 \\ -Fs_3 \\ \sqrt{2}Fc_3 \end{bmatrix}$$

$$+ \left[p^{4*0} + \frac{m - m}{m} r^1 + \frac{m - \bar{m}}{m} r^2 - \frac{1}{m} \bar{\gamma}_{EO}^T M q\right]^{\sim} \frac{1}{\sqrt{2}} \begin{bmatrix} Fs_4 \\ -Fs_4 \\ \sqrt{2} Fc_4 \end{bmatrix}$$

Linearization of this expression and of the right hand side of Eq. (2) about the solution of Eqs. (12) produces the following linearized vehicle equation

$$I\ddot{\theta} + \tilde{\kappa}\ddot{r}^1 + \tilde{\bar{\kappa}}\ddot{r}^2 + I^{5}\ddot{\alpha}^5 + I^{6}\ddot{\alpha}^6 - \bar{\delta}^T\ddot{\bar{\eta}}$$

$$= -(p^{3*0} - p^{4*0})^{\sim} \tilde{F}^2 \alpha_3$$

$$- \frac{3}{m} \tilde{F}^2 [(m - m) r^1 + (m - \bar{m}) r^2 - \bar{\Delta}^T \bar{\eta}] \qquad (15)$$

New symbols are defined as follows

I - vehicle inertia dyadic for the nominal state

$p^{i*0} - \sum_{i=2}^{7} M_i p^{i*0}$

$\bar{\kappa} - \sum_j M_j p^{j*0}$, $j = 2,3,4$

Truncation of all but the first six modes will be adhered to in the sequel. Thus $\bar{\delta}$ and $\bar{\Delta}$ are 6 x 3 matrices. A structural analysis of the entire vehicle reveals that only three of the elements of $\bar{\delta}$ and two of the elements of $\bar{\Delta}$ are non-zero. In particular, $\bar{\delta}$ and $\bar{\Delta}$ have the forms

$$\bar{\delta} = \begin{bmatrix} 0 & \delta_{12} & 0 \\ 0 & 0 & \delta_{23} \\ 0 & 0 & 0 \\ 0 & 0 & 0 \\ \delta_{51} & 0 & 0 \\ 0 & 0 & 0 \end{bmatrix}, \qquad \bar{\Delta} = \begin{bmatrix} 0 & 0 & 0 \\ 0 & 0 & 0 \\ 0 & 0 & \Delta_{33} \\ 0 & \Delta_{42} & 0 \\ 0 & 0 & 0 \\ 0 & 0 & 0 \end{bmatrix}$$

Substitution of these expressions and of those for r^1 and r^2 into Eq. (14) produces the following six scalar equations of motion for the modal coordinates

$$
\begin{aligned}
\ddot{\eta}_1 + 2\zeta_1 \sigma_1 \dot{\eta}_1 + \sigma_1^2 \eta_1 &= \delta_{12} \ddot{\theta}_2 \\
\ddot{\eta}_2 + 2\zeta_2 \sigma_2 \dot{\eta}_2 + \sigma_2^2 \eta_2 &= \delta_{23} \ddot{\theta}_3 \\
\ddot{\eta}_3 + 2\zeta_3 \sigma_3 \dot{\eta}_3 + \sigma_3^2 \eta_3 &= 0 \\
\ddot{\eta}_4 + 2\zeta_4 \sigma_4 \dot{\eta}_4 + \sigma_4^2 \eta_4 &= -\Delta_{42} r \ddot{\alpha}_6 \\
\ddot{\eta}_5 + 2\zeta_5 \sigma_5 \dot{\eta}_5 + \sigma_5^2 \eta_5 &= \delta_{51} \ddot{\theta}_1 \\
\ddot{\eta} + 2\zeta_6 \sigma_6 \dot{\eta}_6 + \sigma_6^2 \eta_6 &= 0
\end{aligned}
\tag{16}
$$

where σ_i and ζ_i are the frequency and damping ratio respectively for the ith mode.

Figure 17 shows the mode shapes and lists the frequencies corresponding to the first six modes.*

The vehicle matrix equation (15) is then equivalent to the three scalar equations

*Provided by Dr. E. Weiner of Division 35, who modeled the structure and made the necessary computer calculations.

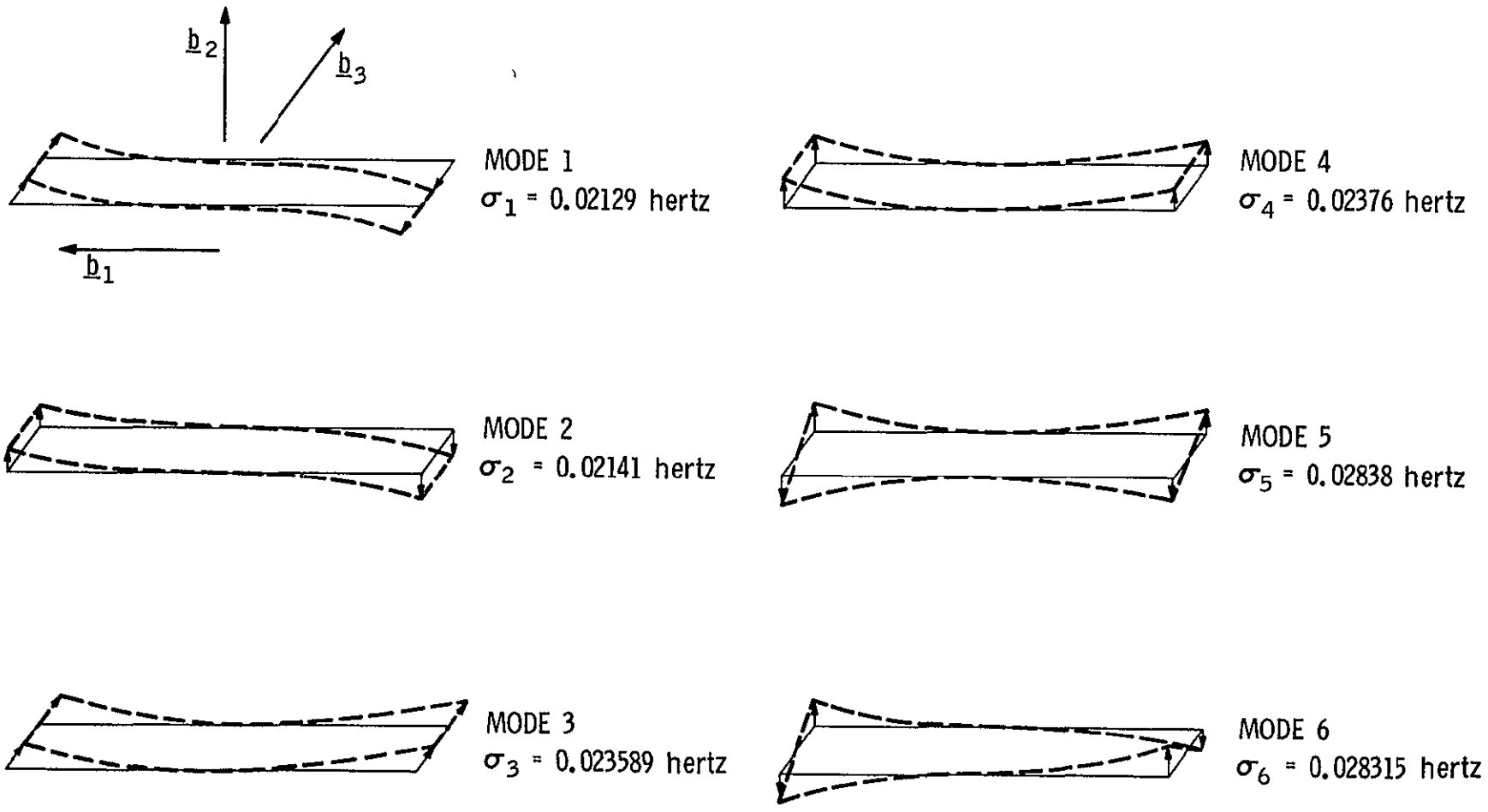

Figure 17. Solar Array Mode Shapes

$$I_1\ddot{\theta}_1 + \bar{\kappa}_3 r\ddot{\alpha}_6 + \delta_{51}\ddot{\eta}_5 = 3\frac{(m-\bar{m})}{m} rF\alpha_6 - \frac{3F\Delta_{42}}{m}\eta_4 \qquad (17)$$

$$I_2\ddot{\theta}_2 - \kappa_3 r\ddot{\alpha}_5 - \delta_{12}\ddot{\eta}_1 = 3\frac{(m-\bar{m})}{m} rF\alpha_5 \qquad (18)$$

$$I_3\ddot{\theta}_3 (\kappa_2 r + I_3^5)\ddot{\alpha}_5 - (\bar{\kappa}_1 r - I_3^6)\ddot{\alpha}_6$$

$$- \delta_{23}\ddot{\eta}_2 = 2\sqrt{2}p_1^{3*0} F\alpha_3 \qquad (19)$$

where I_i is the moment of inertia of the vehicle for $\underline{b}_i$ and for the nominal state, κ_i and $\bar{\kappa}_i$ are the $\underline{b}_i$ measure numbers of κ and $\bar{\kappa}$, and F is the magnitude of the thrust force exerted by any of the three electric propulsion engines.

The assumption that $\alpha_4 = -\alpha_3$ implies that the equation of motion for α_4 may be ignored. The linearized forms of the remainder of Eqs. (8)-(11) are:

$$I_1^3[\ddot{\alpha}_3 + \frac{1}{\sqrt{2}}(\ddot{\theta}_1 + \ddot{\theta}_2)] + d_3\dot{\alpha}_3 - k_3(\alpha_{G1} - \alpha_3) = 0 \qquad (20)$$

$$(I_3^5 + mr^2 + \frac{m^3}{m^2}r^2 - 2\frac{m^2r^2}{m})\ddot{\alpha}_5 + r^2 d_1\dot{\alpha}_5 + k_2\alpha_5$$

$$+ \frac{m^2\bar{m}}{m^2}r^2\ddot{\alpha}_6 - k_2\alpha_{T2} + (\frac{mr\mu}{m} - \mu r)\ddot{\theta}_2 + I_3^5\ddot{\theta}_3 = 0 \qquad (21)$$

$$(I_3^6 + \bar{m}r^2 + \frac{m\bar{m}^2}{m} r^2 - 2\frac{\bar{m}^2}{m}r^2)\ddot{\alpha}_6 + r^2 d_1\dot{\alpha}_6 + k_1\alpha_6$$

$$+ \frac{\bar{m}^2}{m^2} r^2 \ddot{\alpha}_5 - \frac{1}{m}\left(\frac{m\bar{m}}{m} r - \bar{m}r\right)\Delta_{42}\ddot{\eta}_4 - k_1 \alpha_{T1}$$

$$- \left(\frac{\bar{m}r\mu}{m} - \bar{\mu}r\right)\ddot{\theta}_1 + I_3\ddot{\theta}_3 = 0 \qquad (22)$$

Control:

The linear approximation to the control system block diagram for each axis is shown in Figure 18. A celestial sensor detects the value of θ_i. The transfer function for the sensor is $K_{Si}/(\tau_{Si}s+1)$. A constant K_{Vi} is the transfer function for a voltage controlled oscillator while the linear approximation to a stepper motor has the transfer function K_{Mi}/s. The remaining part of the control system is the compensation network. The output from the stepper motor is the desired translation $r\alpha_{T1}$ or $r\alpha_{T2}$, or the desired gimbal angle α_G. The sign associated with V_{Si} is determined by the sign associated with the translating or gimballing controlling term.

A block diagram of the dynamics and control of the entire vehicle is shown in Figure 19. Coupling between the three axes is indicated.

Differential equations associated with the control system are obtainable from Figure 19. They are

$$\tau_{Si}\dot{V}_{Si} + V_{Si} = K_{Si}\theta_i \qquad i = 1, 2, 3 \qquad (23)$$

$$\left.\begin{aligned} r\dot{\alpha}_{T1} &= K_{M1}K_{V1}(V_{S1} - V_{F1}) \\ r\dot{\alpha}_{T2} &= K_{M2}K_{V2}(-V_{S2} - V_{F2}) \end{aligned}\right\} \qquad (24)$$

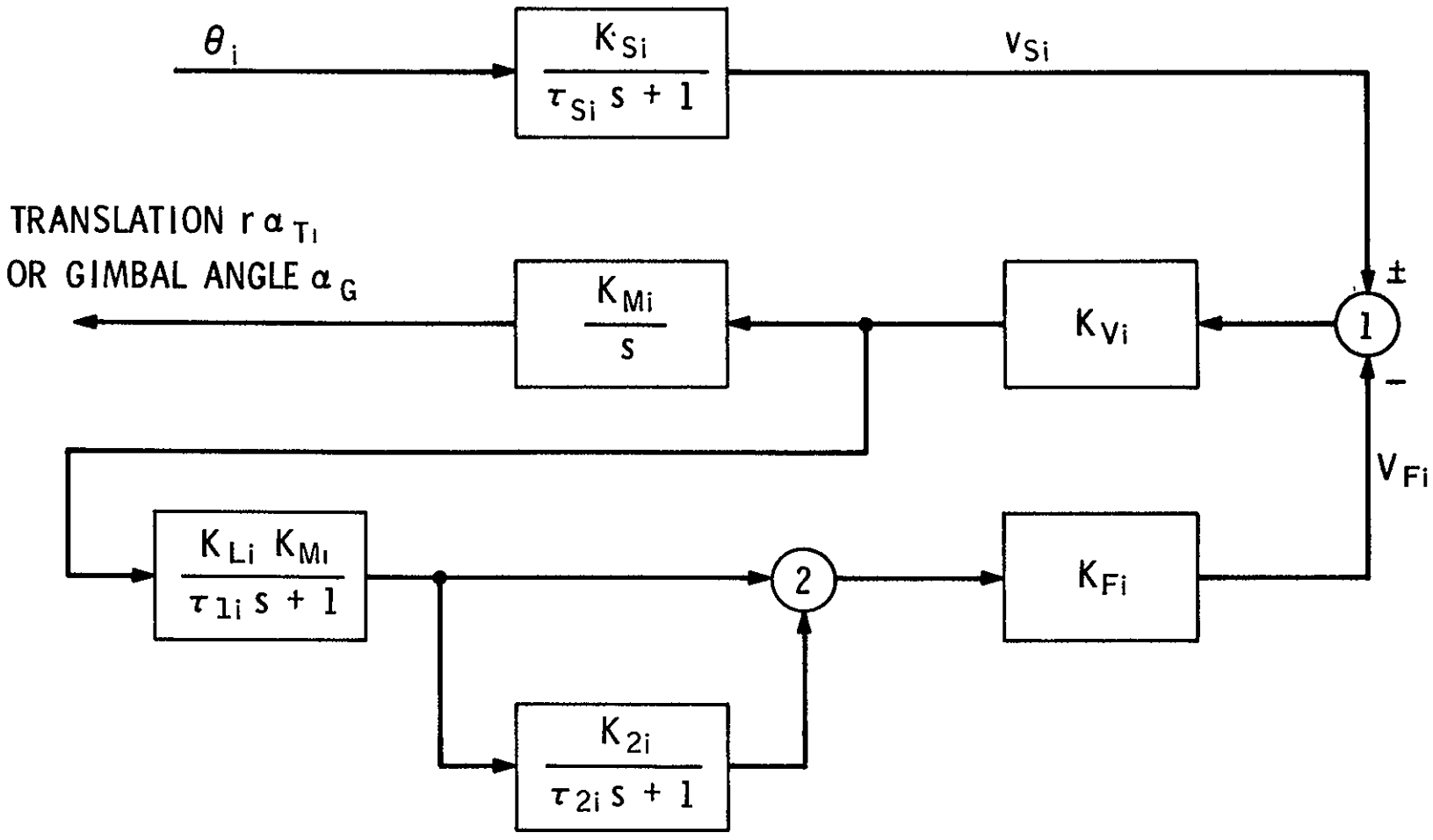

Figure 18. Linear approximation to the control system block diagram

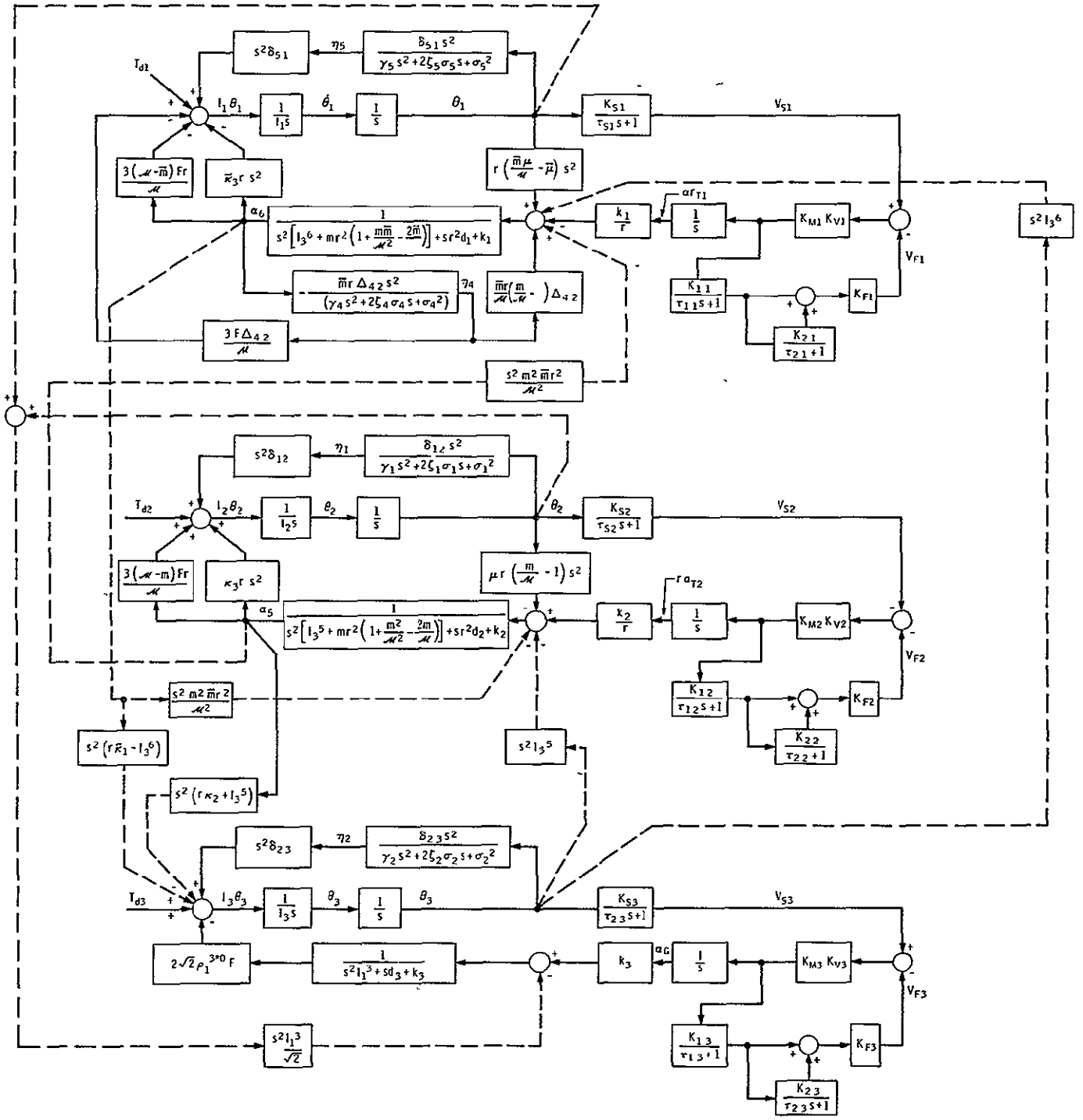

Figure 19. Coupled Three Axis Block Diagram

$$
\left.
\begin{aligned}
\dot{\alpha}_G &= K_{M3}K_{V3}(V_{S3}-V_{F3}) \\
\ddot{V}_{F1} &= \frac{K_{F1}K_{11}K_{M1}K_{V1}}{\tau_{11}\tau_{21}}\Big[\frac{\tau_{21}}{\tau_{S1}}K_{S1}\theta_1 + (1+K_{21}-\frac{\tau_{21}}{\tau_{S1}})V_{S1} \\
&- (\tau_{21} + \frac{\tau_{11}+\tau_{21}}{K_{F1}K_{11}K_{M1}K_{V1}})\dot{V}_{F1} \\
&- (1 + K_{21} + \frac{1}{K_{F1}K_{11}K_{M1}K_{V1}})V_{F1}\Big] \\
\ddot{V}_{F2} &= -\frac{K_{F2}K_{12}K_{M2}K_{V2}}{\tau_{12}\tau_{22}}\Big[\frac{\tau_{22}}{\tau_{S2}}K_{S2}\theta_2 + (1+K_{22}-\frac{\tau_{22}}{\tau_{S2}})V_{S2} \\
&+ (\tau_{22} + \frac{\tau_{12}+\tau_{22}}{K_{F2}K_{12}K_{M2}K_{V2}})\dot{V}_{F2} \\
&+ (1 + K_{22} + \frac{1}{K_{F2}K_{12}K_{M2}K_{V2}})\dot{V}_{F2}\Big] \\
\ddot{V}_{F3} &= \frac{K_{F3}K_{13}K_{M3}K_{V3}}{\tau_{13}\tau_{23}}\Big[\frac{\tau_{13}}{\tau_{S3}}K_{S3}\theta_3 + (1+K_{23}-\frac{\tau_{23}}{\tau_{S3}})V_{S3} \\
&- (\tau_{23} + \frac{\tau_{13}+\tau_{23}}{K_{F3}K_{13}K_{M3}K_{V3}})\dot{V}_{F3} \\
&- (1 + K_{23} + \frac{1}{K_{F3}K_{13}K_{M3}K_{V3}})V_{F3}\Big]
\end{aligned}
\right\} \quad (25)
$$

Stability Analysis:

If the coupling and translator--gimbal dynamics are ignored in Figure 19, then the block diagrams shown in Figures 20-22 result. The drawings at the bottom of each figure indicate the mode or modes which are excited by rotation of the spacecraft about the axis to which the block diagram cor-

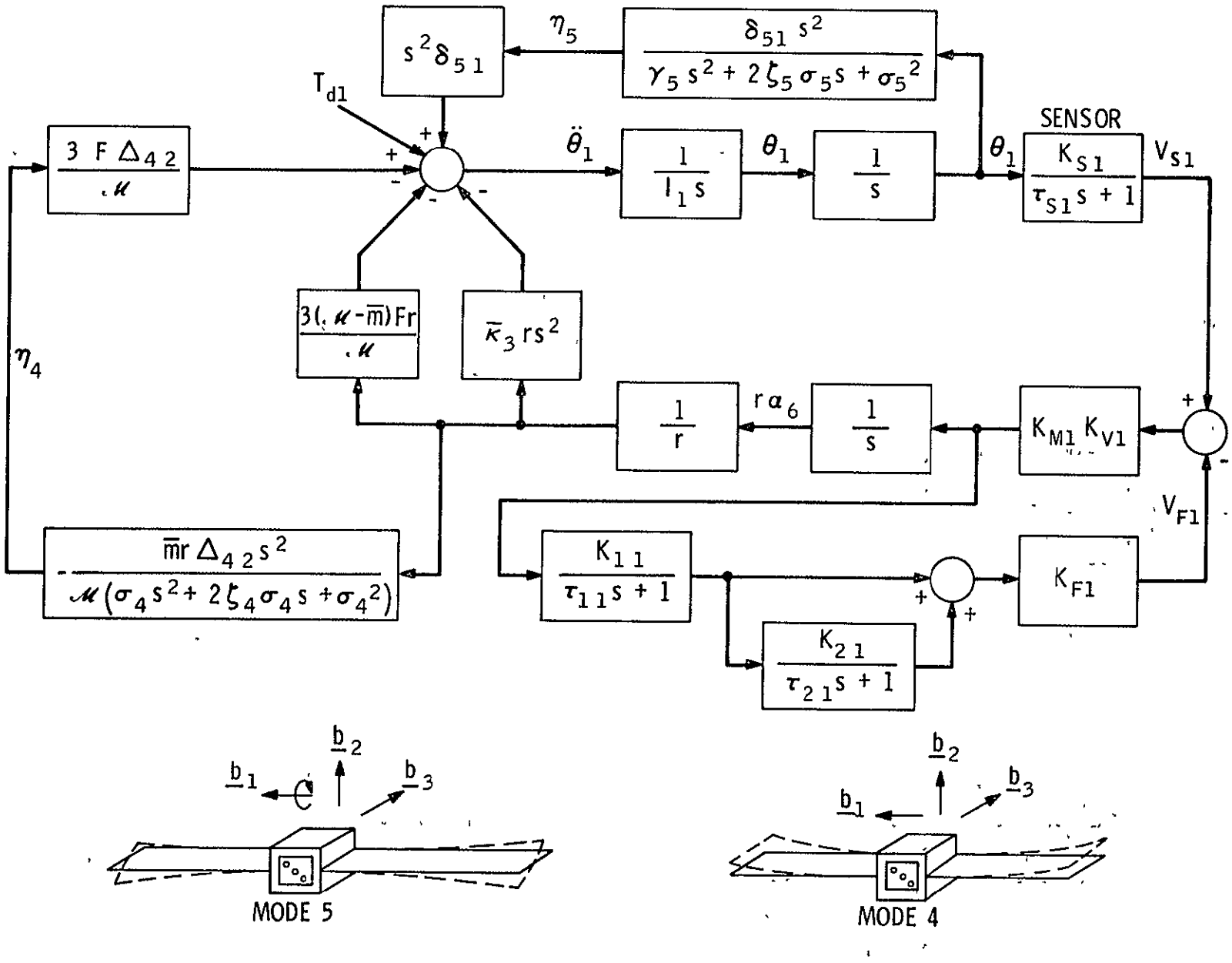

Figure 20. $\underline{b}_1$ Axis Block Diagram

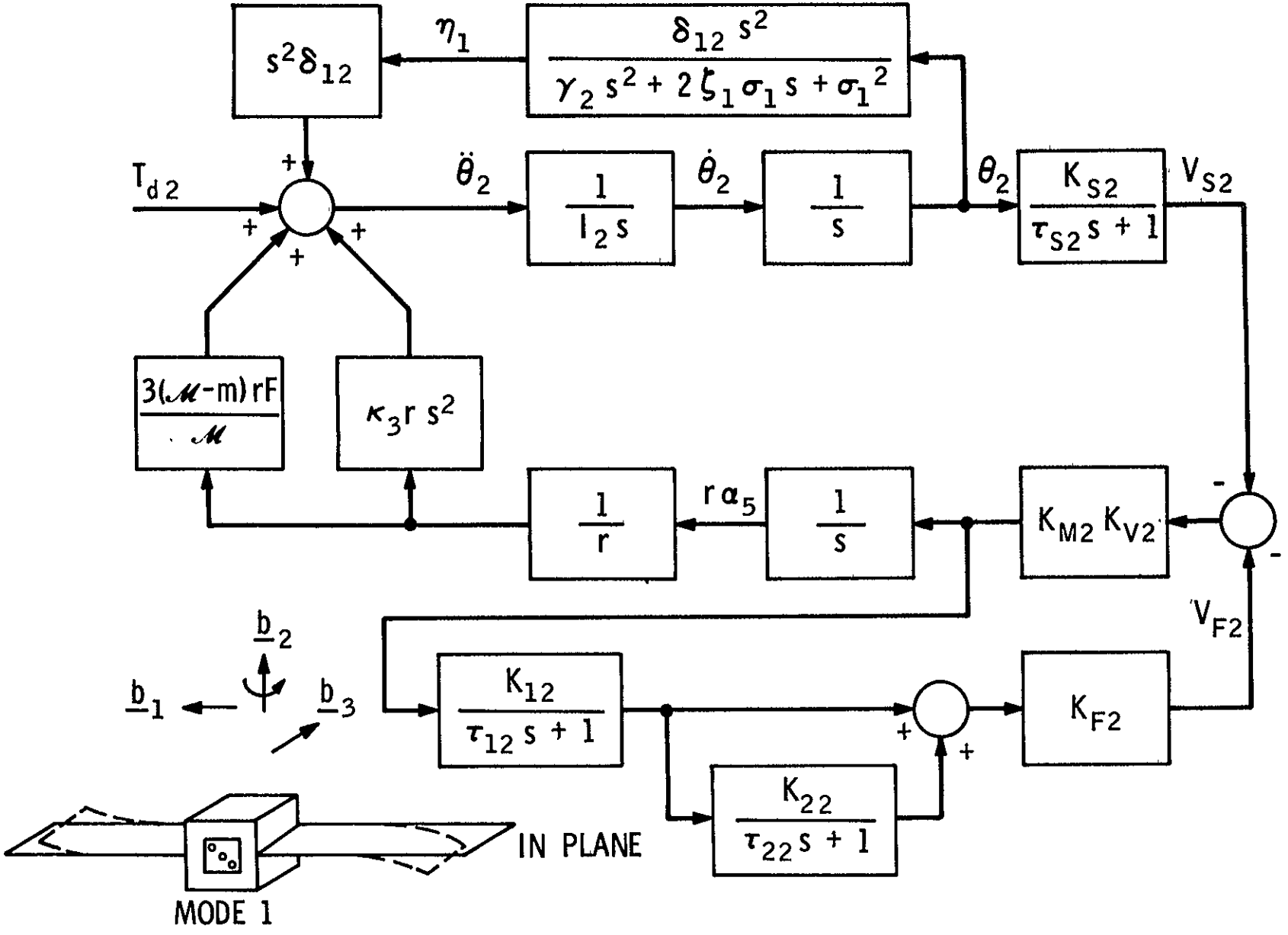

Figure 21. $\underline{b}_2$ Axis Block Diagram

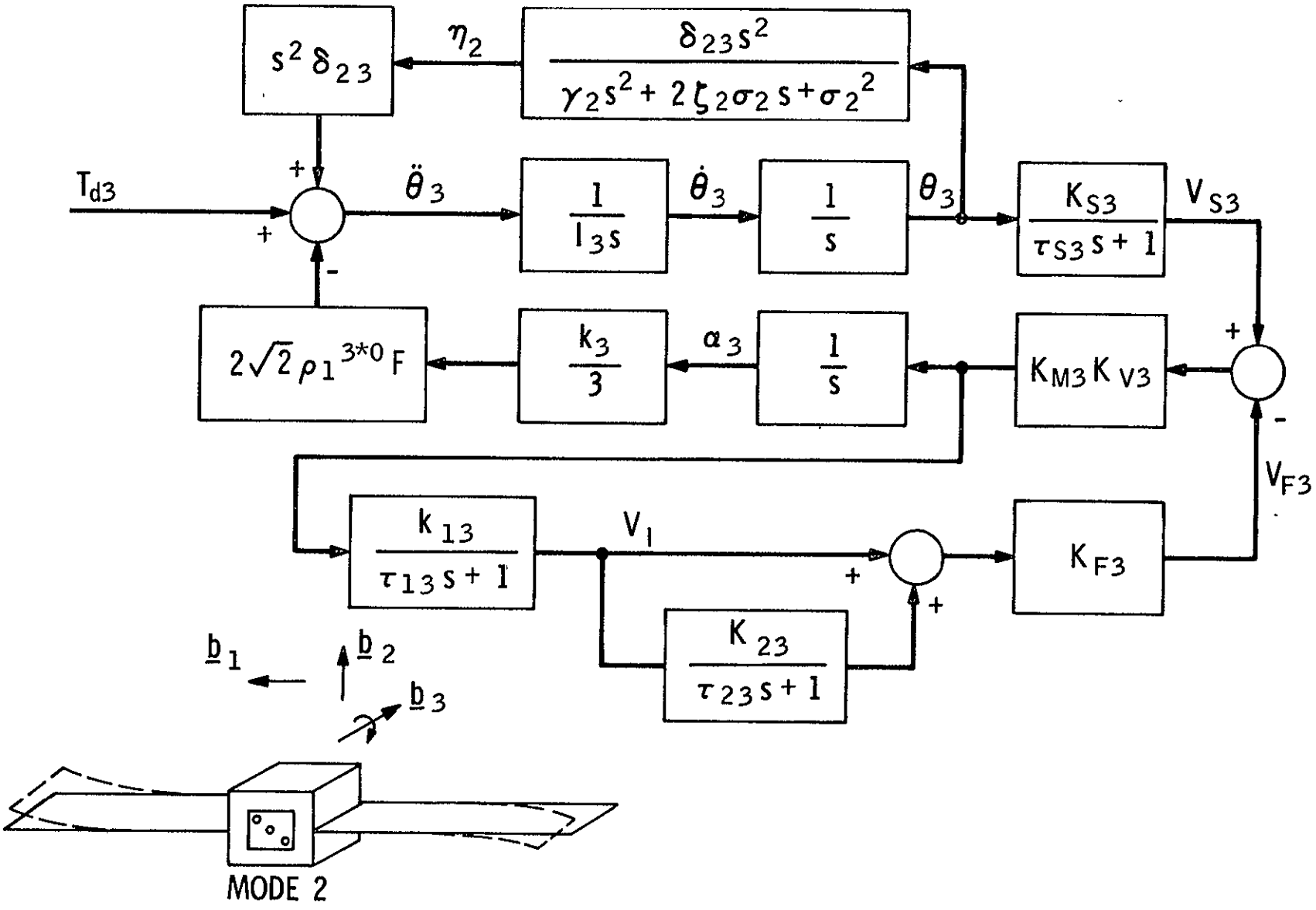

Figure 22. $\underline{b}_3$ Axis Block Diagram

responds. As indicated by Eqs. (16), the third and sixth modes of structural vibration decouple from the remaining equations and consequently have no effect on attitude motion, at least in the linear sense. Uncoupling of the equations transforms the attitude control problem into one that is amenable to root locus analysis.

The open loop transfer functions for the three axes are

$$G_1H_1 = -\bar{K}_3K_{S1}K_{M1}K_{V1}(s^2 + N_5s^5 + N_4s^4 + N_3s^3 + N_2s^2 + N_1s + N_o)(s + 1/\tau_{21})(s + 1/\tau_{11})/(I_1 - \delta_{51}^2)\tau_{S1}s^3(s^4 + D_3s^3 + D_2s^2 + D_1s + D_o)(s + 1/\tau_{S1})\{s^2 + \frac{1}{\tau_{21}\tau_{11}}[\tau_{11} + (1 + K_{11}K_{M1}K_{V1}K_{F1})\tau_{21}]s + \frac{1}{\tau_{21}\tau_{11}} + \frac{K_{11}K_{M1}K_{V1}K_{F1}}{\tau_{21}\tau_{11}}(1 + K_{21})\} \quad (26)$$

$$G_2H_2 = -\frac{K_3K_{S2}K_{M2}K_{V2}}{(I_2-\delta_{12}^2)\tau_{S2}}[s^2 + 3\frac{(m-m)}{K_3m}F](s^2 + 2s\zeta_1\sigma_1 + \sigma_1^2)(s + 1/\tau_{22})(s + 1/\tau_{12})/s^3(s^2 + \frac{2I_2}{I_2 - \delta_{12}^2}\zeta_1\sigma_1 s + \frac{I_2\sigma_1^2}{I_2 - \delta_{12}^2})(s + 1/\tau_{S2})\{s^2 +$$

$$\frac{1}{\tau_{22}\tau_{12}}[\tau_{12} + (1 + K_{21}K_{M2}K_{V2}K_{F2})\tau_{22}]s$$

$$+ \frac{1}{\tau_{22}\tau_{12}} + \frac{K_{12}K_{M2}K_{V2}K_{F2}}{\tau_{22}\tau_{12}}(1 + K_{22})\} \qquad (27)$$

$$G_3H_3 = -\frac{\sqrt{8}\, p_1^{3*}O_{FK_{S3}K_{M3}K_{V3}}}{(I_3 - \delta_{23}^2)\tau_{S3}}(s^2 + 2\zeta_2\sigma_2 s + \sigma_2^2)(s +$$

$$1/\tau_{23})(s + 1/\tau_{13})/s^3(s^2 + \frac{2I_3\zeta_2\sigma_2}{I_3-\delta_{23}^2}s + \frac{I_3\sigma_2^2}{I_3-\delta_{23}^2})$$

$$(s + 1/\tau_{S3})\{s^2 + \frac{1}{\tau_{23}\tau_{13}}[\tau_{13} + (K_{M3}K_{F3}K_{13}K_{V3} + 1)\tau_{23}]s$$

$$+ \frac{1}{\tau_{23}\tau_{13}} + \frac{K_{F3}K_{M3}K_{13}K_{V3}}{\tau_{23}\tau_{13}}(1 + K_{23})\} \qquad (28)$$

where G_i is the forward loop transfer function and H_i is the feedback loop transfer function. Expressions for N_i, i=0,...,5 and for D_J, J=0,...,3 are

$$N_5 = 2(\zeta_4\sigma_4 + \zeta_5\sigma_5)$$

$$N_4 = \sigma_4^2 + \sigma_5^2 + 4\zeta_4\zeta_5\sigma_4\sigma_5 + \frac{3(\mathfrak{M}-\bar{m})F}{\bar{K}_3\mathfrak{M}}$$

$$- 3 \frac{F\bar{m}\Delta_{42}^2}{\bar{\kappa}_3 m^2}$$

$$N_3 = 2\sigma_4\sigma_5(\zeta_4\sigma_5 + \zeta_5\sigma_4) + 6\frac{(m - \bar{m})F}{\bar{\kappa}_3 m}(\zeta_4\sigma_4 + \zeta_5\sigma_5)$$

$$- \frac{6F\bar{m}\Delta_{42}^2\zeta_5\sigma_5}{\bar{\kappa}_3 m^2}$$

$$N_2 = \sigma_4^2\sigma_5^2 + \frac{3(m - m)}{\bar{\kappa}_3 m}(\sigma_4^2 + \sigma_5^2 + 4\zeta_4\zeta_5\sigma_4\sigma_5)$$

$$- \frac{3F\bar{m}\Delta_{42}^2\sigma_5^2}{\bar{\kappa}_3 m^2}$$

$$N_1 = \frac{6(m - \bar{m})F\sigma_4\sigma_5}{\bar{\kappa}_3 m}(\zeta_4\sigma_5 + \zeta_5\sigma_4)$$

$$N_0 = \frac{3(m - \bar{m})F\sigma_4^2\sigma_5^2}{\bar{\kappa}_3 m} \qquad (29)$$

and

$$D_3 = \frac{I_1}{I_1 - \delta_{51}^2}\left[2(\zeta_4\sigma_4 + \zeta_5\sigma_5) - \frac{2\delta_{51}^2\zeta_4\sigma_4}{I_1}\right]$$

$$D_2 = \frac{I_1}{I_1 - \delta_{51}^2}\left(\sigma_4^2 + \sigma_5^2 + 4\zeta_4\zeta_5\sigma_4\sigma_5 - \frac{\delta_{51}^2\sigma_4^2}{I_1}\right)$$

$$D_1 = \frac{2I_1\sigma_4\sigma_5}{I_1 - \delta_{51}^2}(\zeta_4\sigma_5 + \zeta_5\sigma_4)$$

$$D_0 = \frac{I_1\sigma_4^2\sigma_5^2}{I_1 - \delta_{51}^2} \qquad (30)$$

The values selected for the parameters in these expressions as well as for the parameters in Eqs. (26)-(28) are

K_{1i} = (328 volt seconds/meter) $\quad i = 1, 2, 3$

K_{2i} = 4.5 $\quad i = 1, 2, 3$

K_{Fi} = 80 $\quad i = 1, 2, 3$

$K_{M1} = K_{M2}$ = (6.7×10^{-5} meter/pulse

K_{M3} = 10^{-4} radian/pulse $\quad i = 1, 2, 3$

K_{Vi} = 40 pulses/volt second $\quad i = 1, 2, 3$

δ_{23} = (128.2 Kg m^2)

δ_{12} = (128.3 Kg m^2)

δ_{51} = (9.609 Kg m^2)

Δ_{42} = (13.69 Kg m)

ζ_i = (.006 $Kg^{\frac{1}{2}}$ m) $\quad i = 1, 2, 4, 5$

σ_1 = (.02479 x 2π $Kg^{\frac{1}{2}}$ m/second)

σ_2 = (.02493 x 2π $Kg^{\frac{1}{2}}$ m/second)

σ_4 = (.02767 x 2π $Kg^{\frac{1}{2}}$ m/second)

σ_5 = (.03305 x 2π $Kg^{\frac{1}{2}}$ m/second)

τ_{1i} = 10^3 seconds

τ_{2i} = 5 x 10^2 seconds

τ_{Si} = 1 second

F = (.09 Newton)

I_1 = (442.7 Kg m^2)

I_2 = (12777.0 Kg m^2)

I_3 = (12408.0 Kg m^2)

= (600.0 Kg)

m = (54.41 Kg)

$\bar{m}$ = (45.35 Kg)

$\bar{k}_3$ = (-41.47 Kg m)

k_3 = (-34.55 Kg m)

The sensor gains K_{Si} have not been specified and will serve as variable parameters upon which the attitude stability depends.

The root locus for the $\underline{b}_1$ axis is shown in Figure 23. Open loop poles and zeros corresponding to the $\underline{b}_1$ axis case are listed. The poles and zeros having non-zero imaginary parts are associated with the fourth and fifth flexibility modes. A real zero at 0.084324 is due to the so-called "tail-

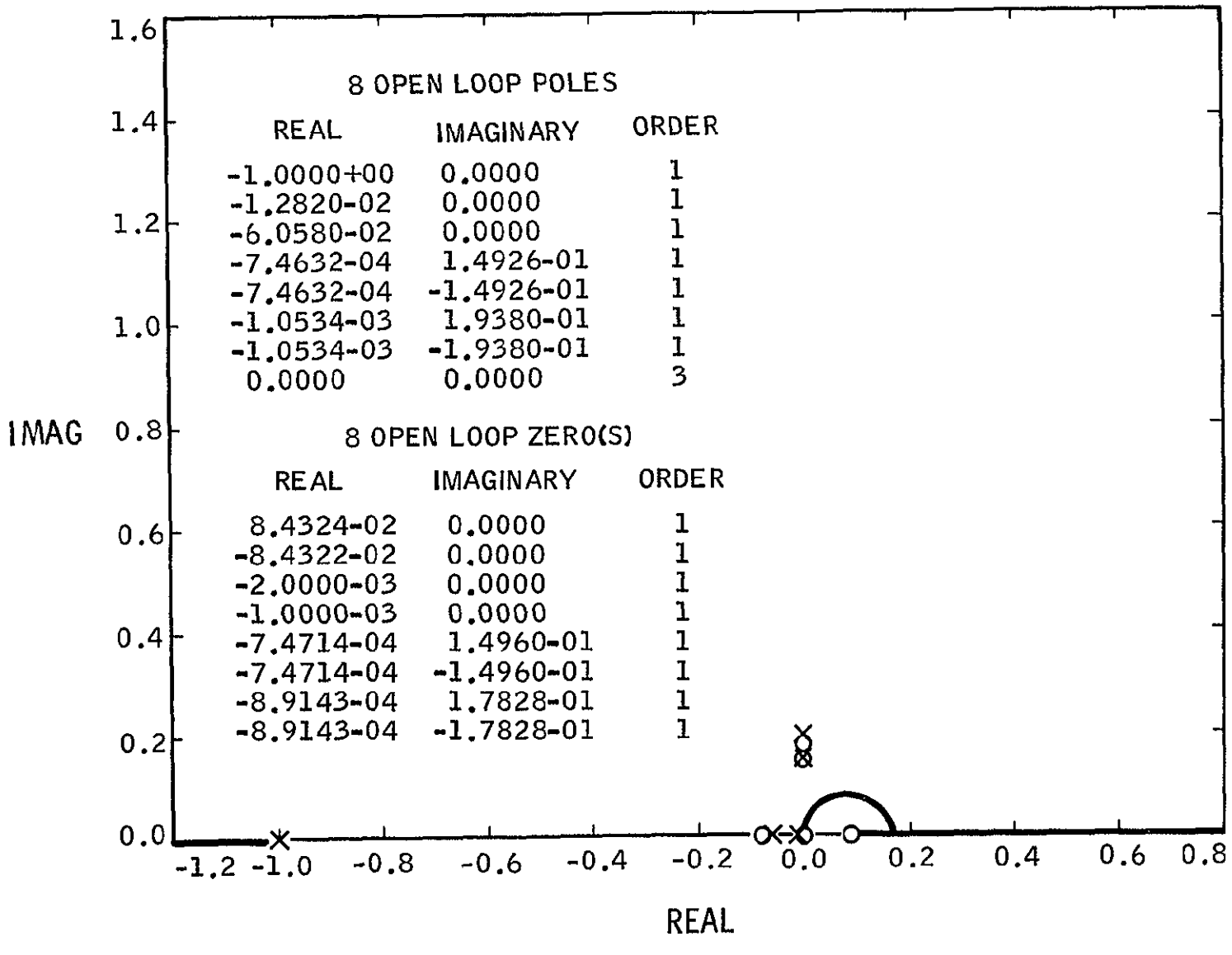

Figure 23. $\underline{b}_1$ Axis Root Locus, Fourth and Fifth Mode Flexibility

wags-dog effect" or the term $\bar{K}_3 r\ddot{\alpha}_6$ in Eq. (17). This is an inertia torque exerted on the vehicle when the engine cluster unit translates in the $\underline{b}_2$ direction. Such translation activates fourth mode oscillations. Figure 24 is an enlarged version of Figure 23 and shows detail near the origin. For very small gain, i.e., very small K_{S1}, the locus emanating from the multiple pole at zero initially passes into the right half-plane. Thus, instability is implied. As K_{S1} is increased, the locus crosses back into the left half-plane and finally returns to the right half-plane for sufficiently large K_{S1}. That part of the locus which corresponds to flexibility traces a path from the left half-plane into the right and then back to the left half-plane. The range of K_{S1} for which all parts of the locus lie in the left half-plane is $0.50 < K_{S1} < 23.0$. For the case when flexibility is ignored and the vehicle is assumed to be rigid, the stability range for K_{S1} is $0.52 < K_{S1} < 23.52$.

Figure 25 shows the root locus for the axis parallel to $\underline{b}_2$. As before, the poles and zeros not on the real axes are flexibility poles and zeros. Also, for very small gain, the locus traced from the multiple pole at zero passes into the right half-plane. As K_{S2} is increased, the locus moves into the left half-plane, then to the right and finally to the left of the imaginary axis. A part of the locus associated with the flexibility pole begins in the left half-plane and soon moves to the right half-plane. Stability for the $\underline{b}_2$ axis is guaranteed for $15 < K_{S2} < 201$. For comparison, Figure 26 shows a root locus for the $\underline{b}_2$ axis when the vehicle is assumed to be rigid. The character of the locus in Figure 26 differs considerably from that in Figure 27. It was determined for the rigid model that the

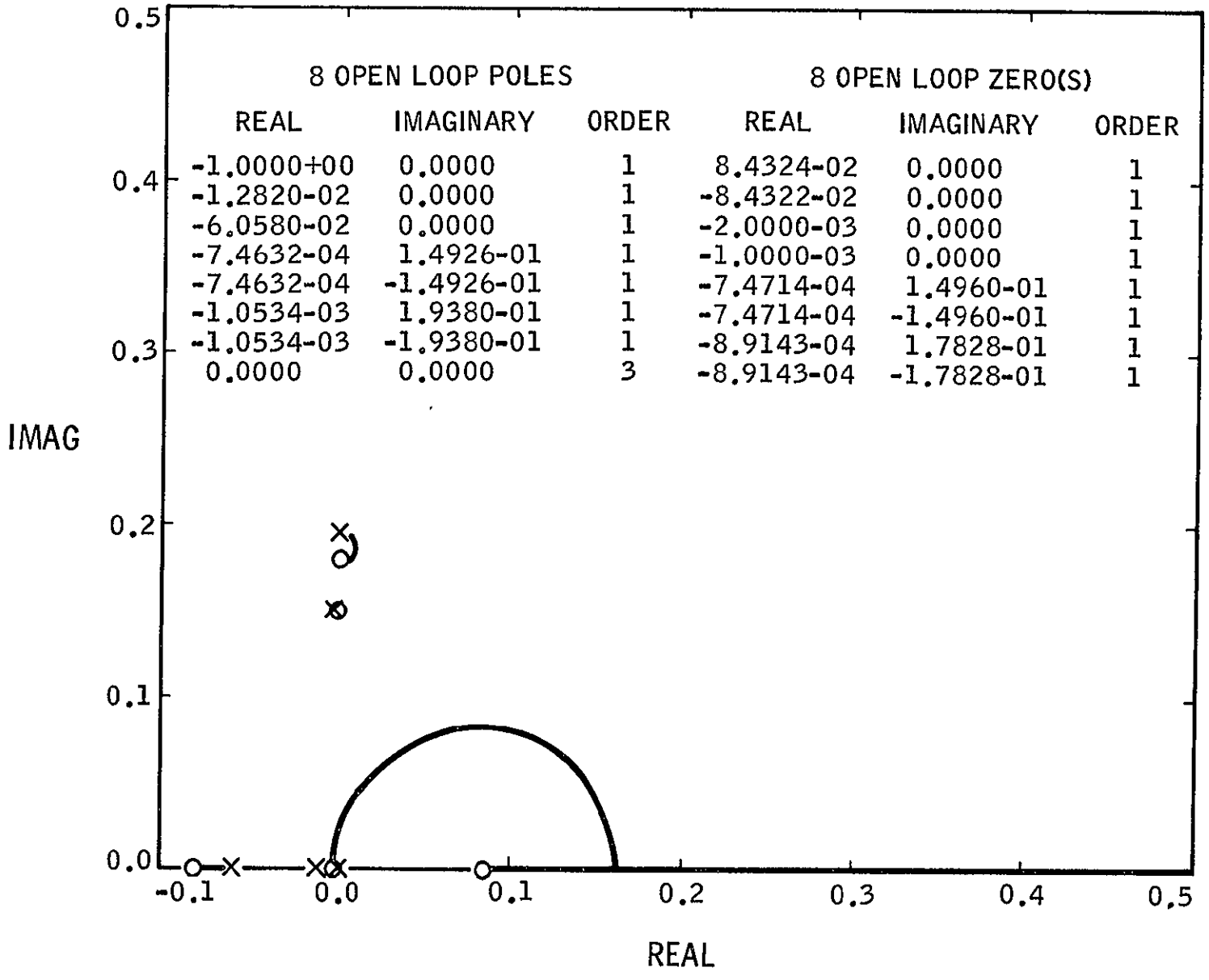

Figure 24. $\underline{b}_1$ Axis Root Locus

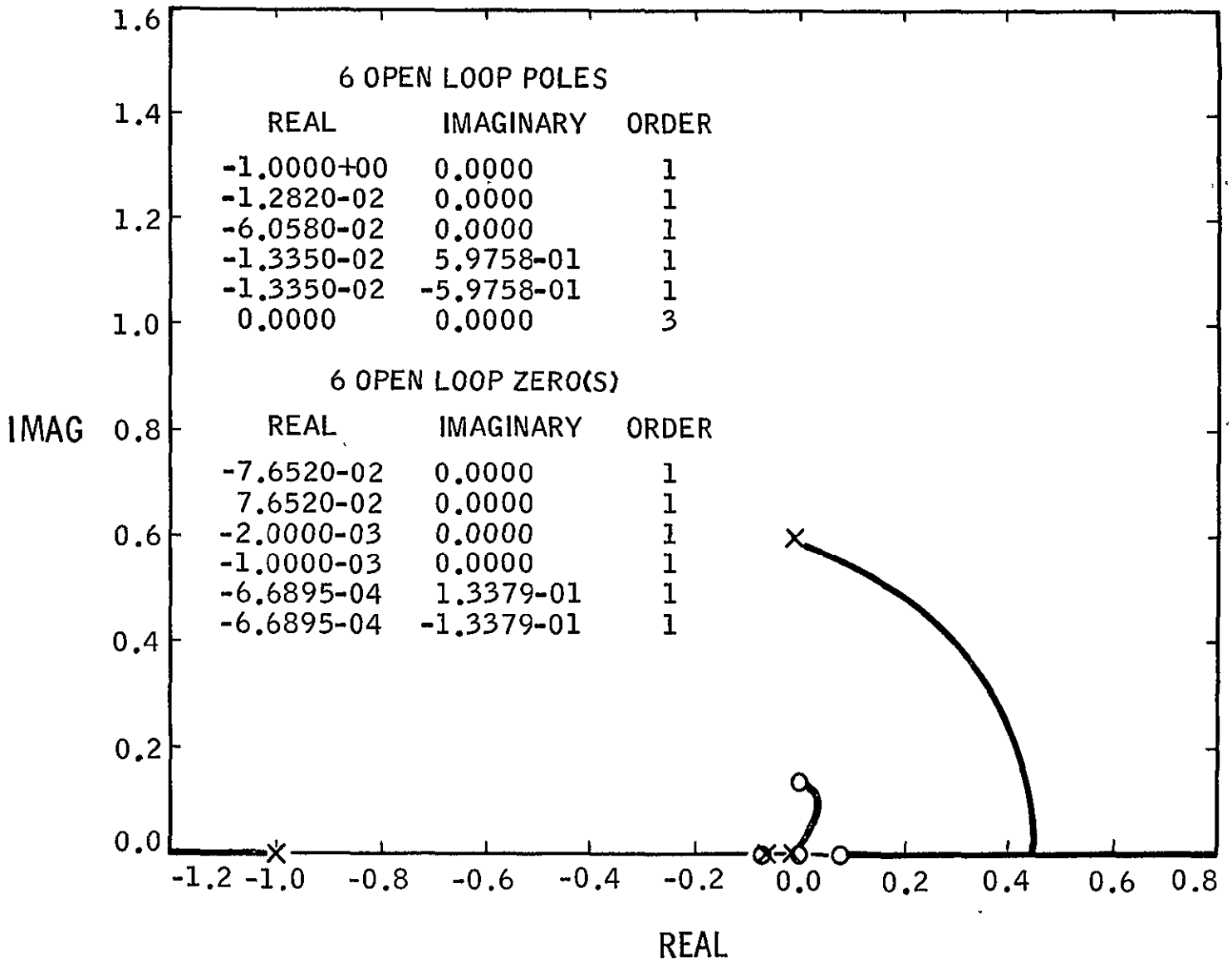

Figure 25. $\underline{b}_2$ Axis Root Locus, First Mode Flexibility

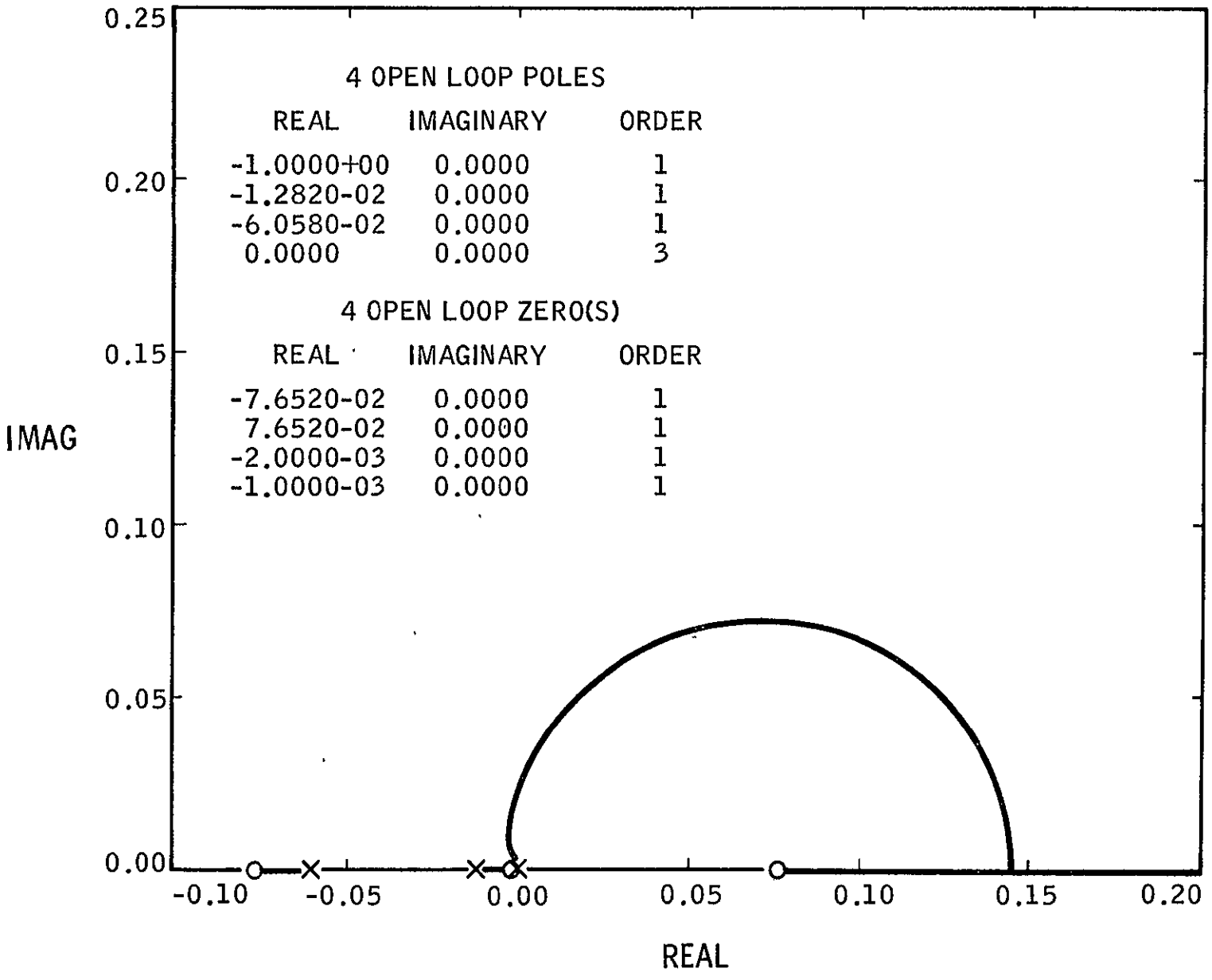

Figure 26. $\underline{b}_2$ Axis Root Locus, Rigid Vehicle

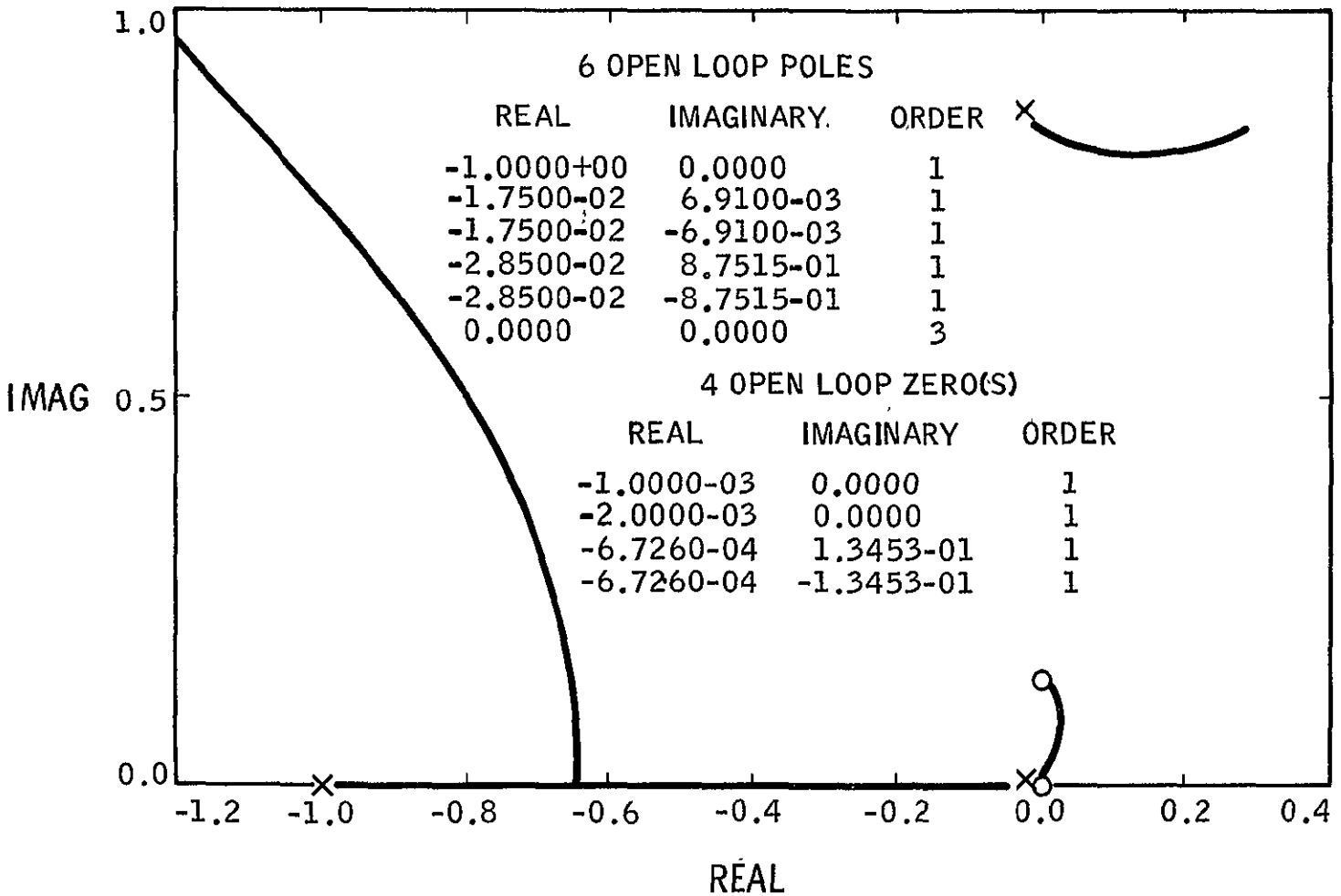

Figure 27. $\underline{b}_3$ Axis Root Locus, Second Mode Flexibility

range of K_{S2} which will ensure stability is $16 < K_{S2} < 276$. Thus, the flexible nature of the solar array is detrimental to the attitude stability of the $\underline{b}_2$ axis.

The final root locus corresponds to the axis parallel to $\underline{b}_3$. There is no "tail-wags-dog" term for this axis, and this is reflected in the absence of a zero on the positive real axis. As in the case of the $\underline{b}_2$ axis, there is only one flexibility pole and one flexibility zero. Values of K_{S3} for which stable attitude motions are guaranteed are $11 < K_{S3} < 221$ for both the flexible spacecraft model and for the rigid model.

Time histories of the attitude angles θ_1, θ_2, and θ_3 appear in Figures 28-33. The CSSL simulation language, developed through the support of the Guidance and Control Branch of the Office of Advanced Research and Technology, was used in programming the linear equations for the UNIVAC 1108 digital computer. For the axis parallel to $\underline{b}_i$, the initial attitude angle rate $\dot{\theta}_1$ is 10^{-4} radian per second. This rate is considerably larger than those expected to be encountered from disturbance torques for a deep space mission. All other variables, i.e., θ_i, V_{Si}, etc., have an initial value of zero. Figures 28-30 show the attitude behavior for cases when K_{Si}, $i = 1, 2, 3$ is in the stable range stated earlier. In particular, $K_{S1} = 20$, $K_{S2} = 100$, $K_{S3} = 100$.

At approximately 100 seconds, θ_1 reaches its maximum amplitude of 6.4×10^{-3} radian. For a time of 2800 seconds, the amplitude has diminished to nearly 7×10^{-4} radian or one-tenth the maximum aplitude. For θ_2 and θ_3, the response curves are of a lower frequency than for θ_1. This is probably a reflection of the small inertia I_1 in comparison with I_2 or I_3.

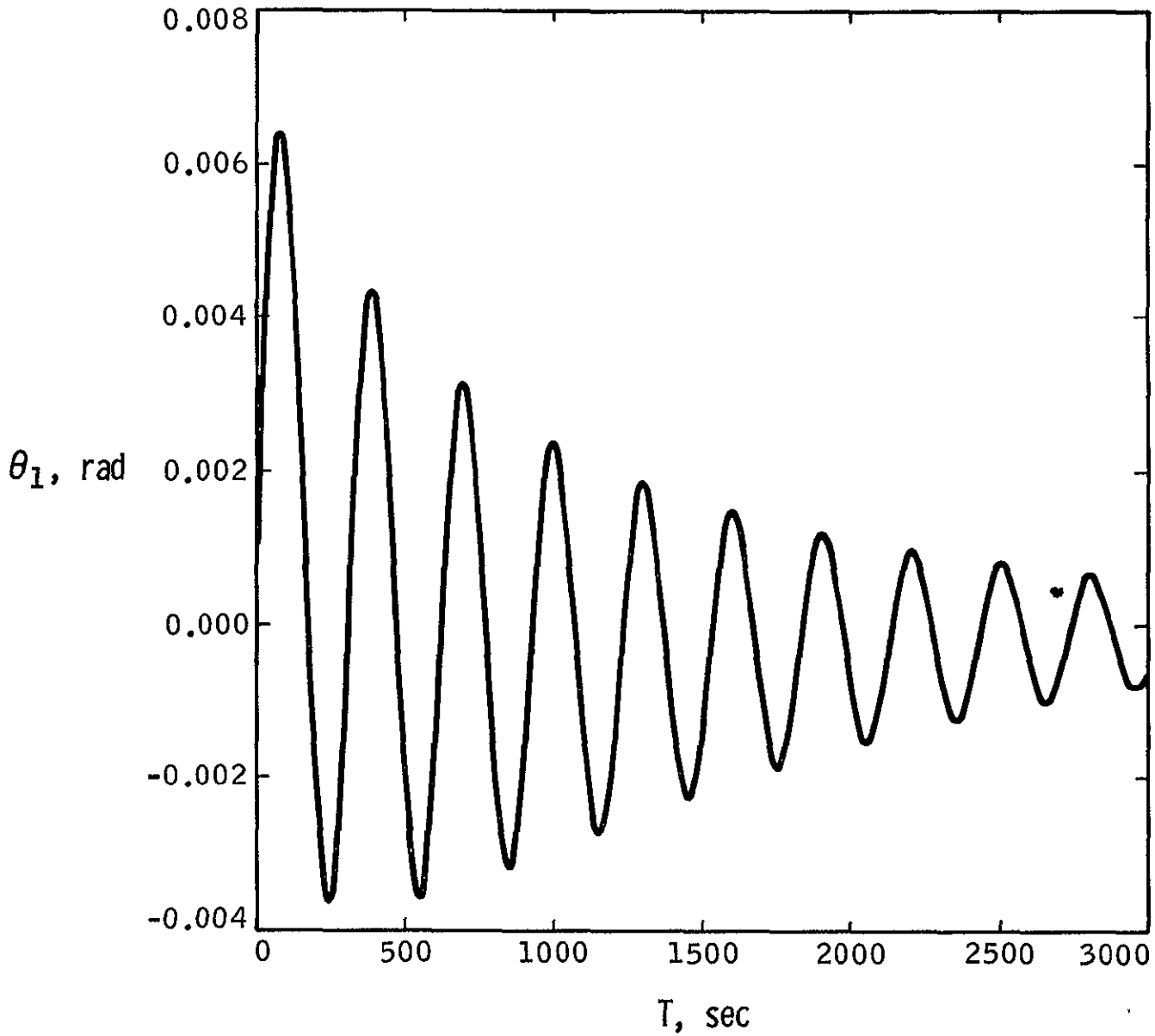

Figure 28. θ_1 Response, $K_{S1} = 20.0$

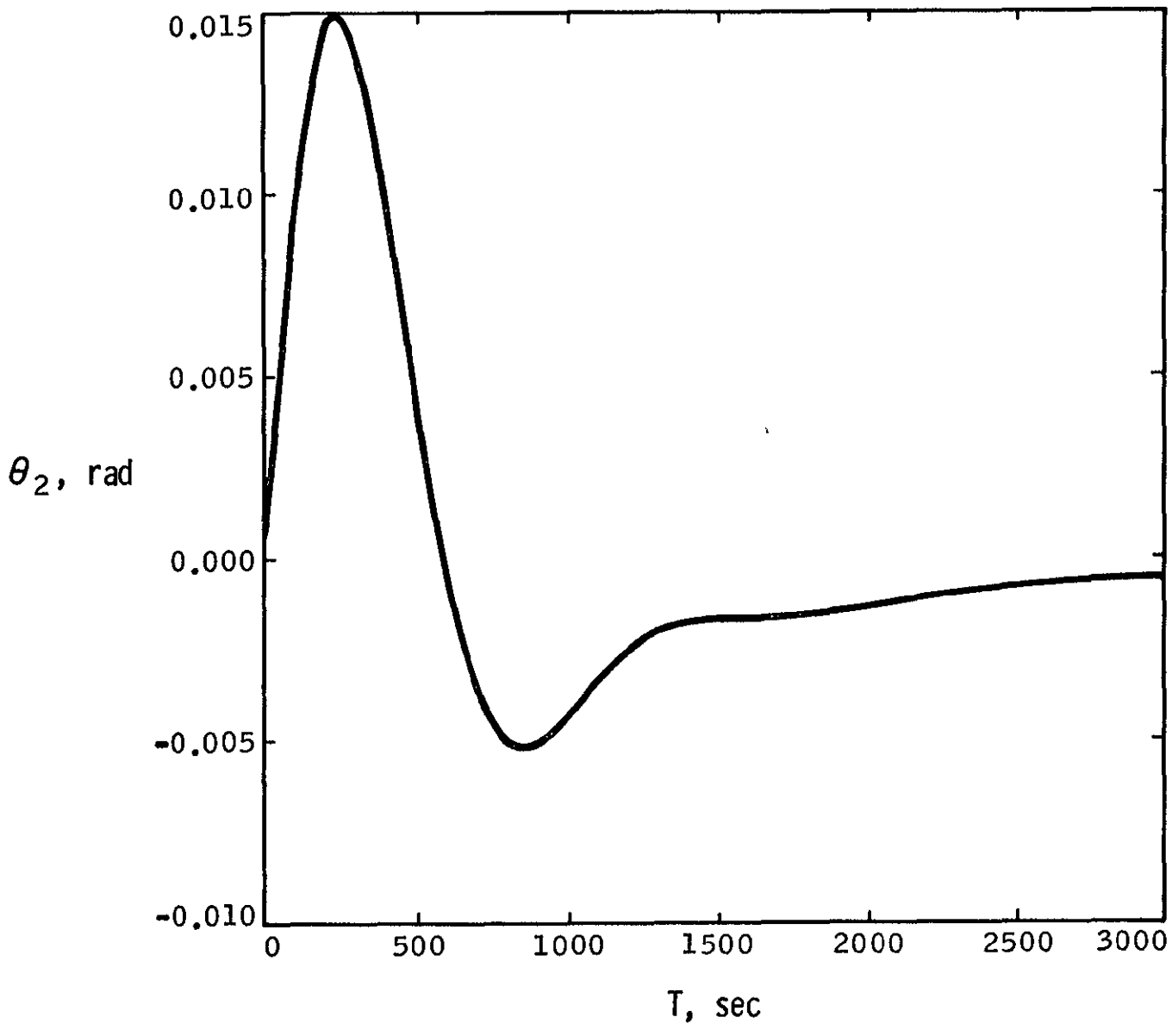

Figure 29. θ_2 Response, K_{S2} = 100.0

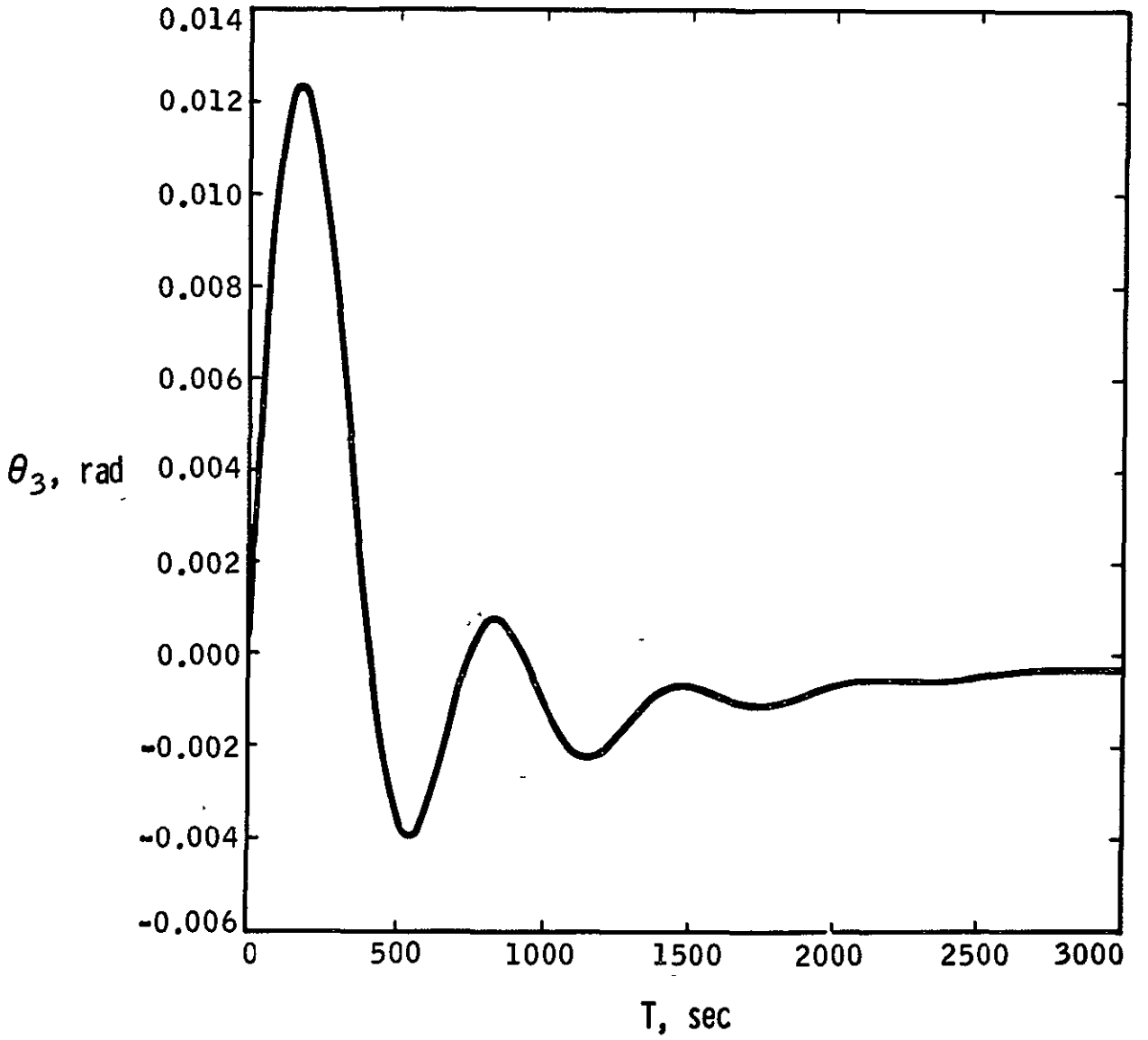

Figure 30. θ_3 response, $K_{S3} = 100.0$

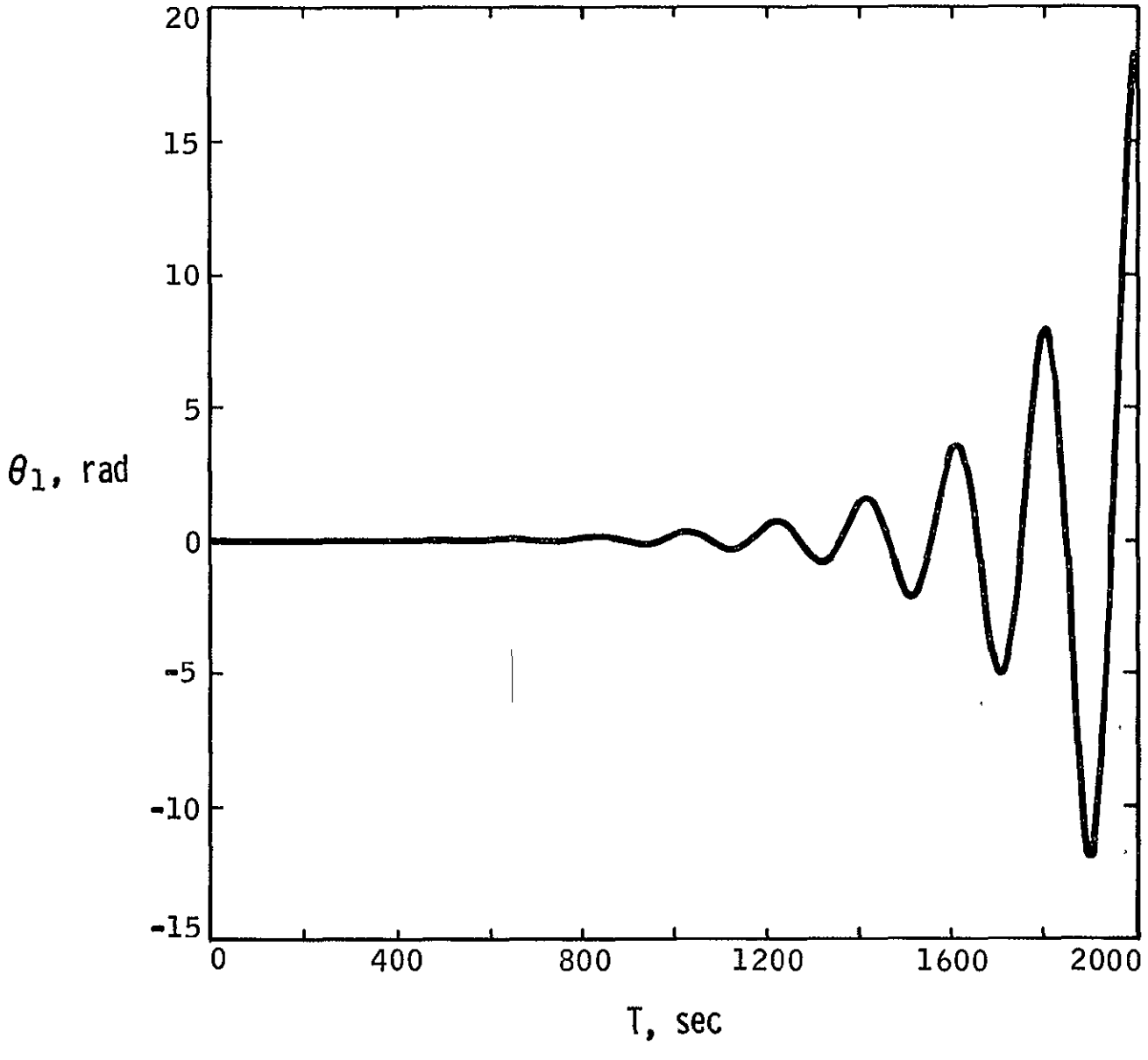

Figure 31. θ_1 Response, $K_{S1} = 50.0$

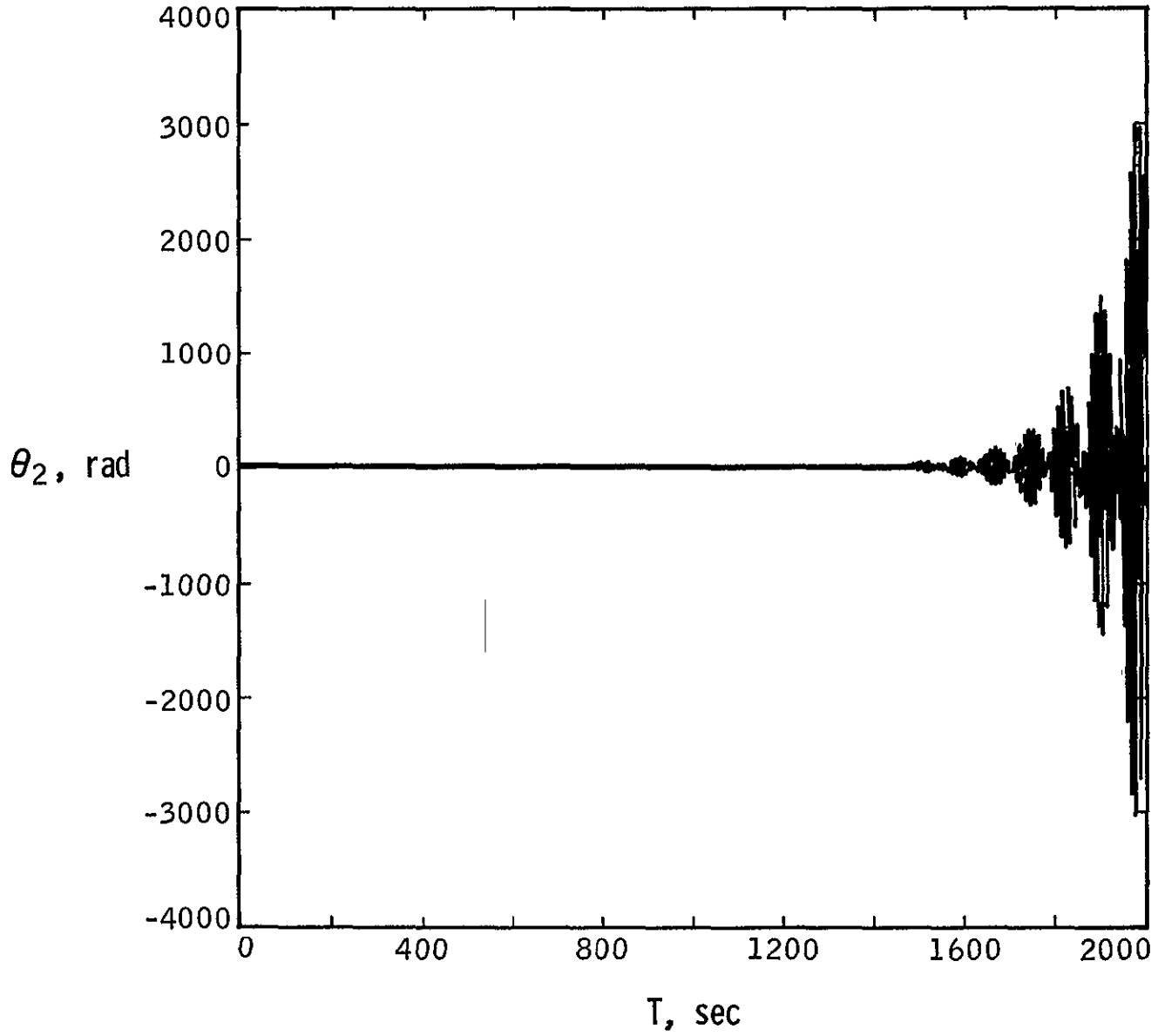

Figure 32. θ_2 Response, K_{S2} = 350.0

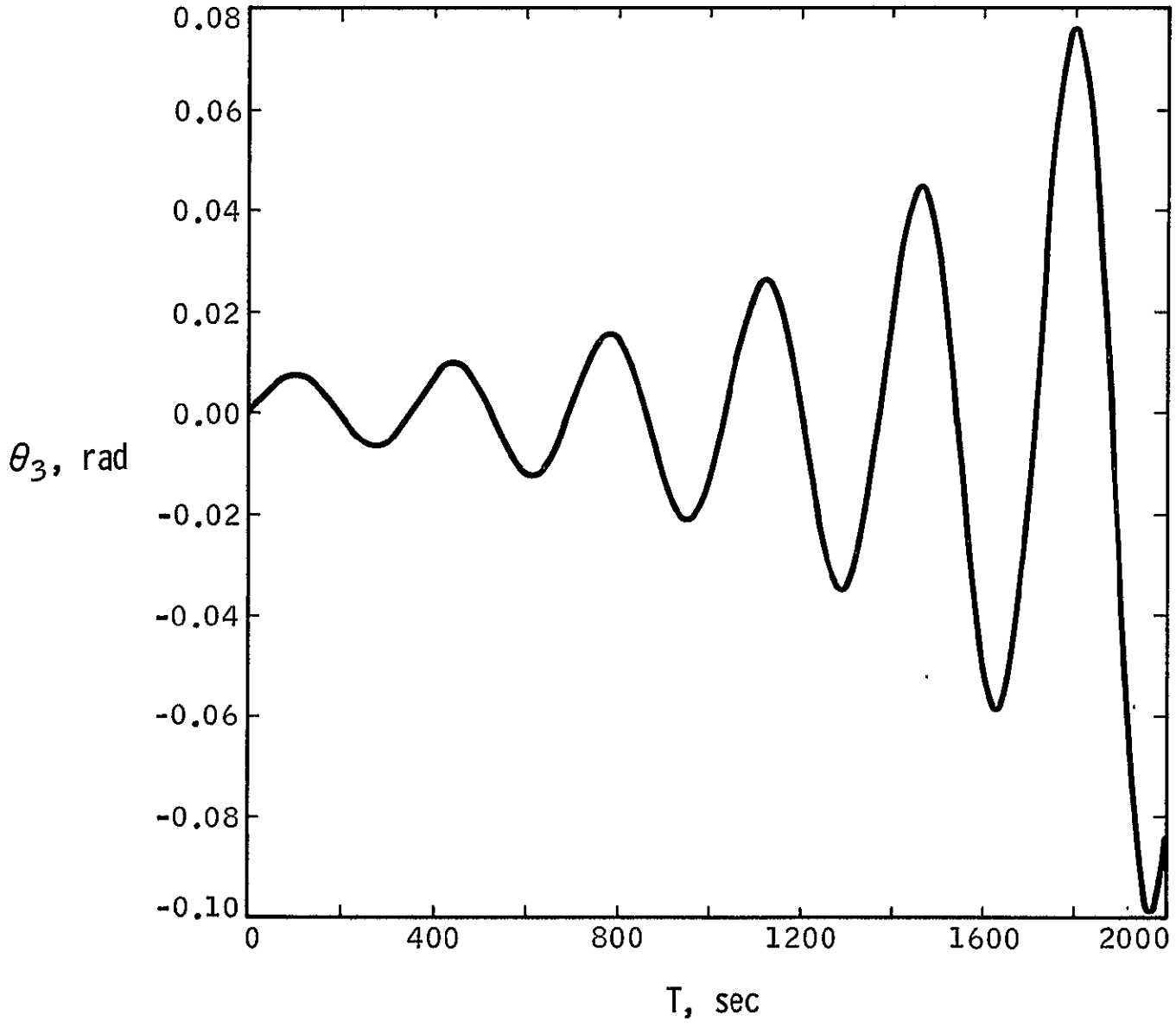

Figure 33. θ_3 Response, K_{S3} = 350.0

Values for K_{S1}, K_{S2}, and K_{S3} in Figures 31-33 are 50, 350, and 350 respectively. These fall outside of the stable ranges. The θ_i responses are then expected to be unstable. This is seen to be the case. However, the curves are not reliable as true indicators of the behavior of θ_i since the linear equations are not really valid for large θ_i. θ_i is indeed unstable, but its time history probably departs markedly from the curves of Figures 31-33.

Conclusions:

The work presented here has demonstrated the feasibility of using electric propulsion engines for attitude control as well as for propulsion during the low-thrust cruise phase of a deep space mission. In addition, it has been shown that flexibility associated with large roll-out solar arrays poses no great threat to the success of such missions. Furthermore, the detrimental effects from torques due to "tail-wags-dog" terms can be offset.

Structural frequencies of the order of 0.025 cycles per second were encountered for the solar arrays. Only for the axis of maximum inertia, the one parallel to $\underline{b}_2$, did the structural influence have a pronounced influence on the rigid body stability characteristics. There, the permissable operating range for K_{S2} was reduced from $16 < K_{S2} < 276$ to $15 < K_{S2} < 201$. Little or no change in the rigid spacecraft stability ranges for K_{S1} and K_{S3} was encountered from structural effects. This was the case despite the fact that for the $\underline{b}_1$ axis, two modes of flexible motion were activated.

For the unstable cases, the θ_2 response seemed to have a growth rate far in excess of the θ_1 or θ_3 responses. A possible explanation for this is that I_2 is greater than either I_1 or I_3 and consequently, the control

system is attempting to handle a large inertia torque $-I_2\ddot{\theta}_2$. Actually, I_3 is very nearly the same as I_2. However, in addition to the inertia torque, the $\underline{b}_2$ control system must contend with the "tail-wags-dog" effect which is absent in the $\underline{b}_3$ dynamics. The $\underline{b}_1$ axis unstable response seems to be intermediate to the $\underline{b}_2$ and $\underline{b}_3$ axes responses. Even though I_1 is quite small when compared to I_2 or I_3, there is a "tail-wags-dog" effect for this axis. Thus, it appears that outside of the stable operating ranges, the "tail-wags-dog" influence is felt very strongly.

REFERENCES: (1) Likins, P. W., "Dynamics and Control of Flexible Space Vehicles," JPL TR 32-1329, Rev. 1, January 15, 1970.

(2) Marsh, E. L., "The Attitude Control of a Flexible Solar Electric Spacecraft," AIAA Paper No. 70-1140, presented at AIAA 8th Electric Propulsion Conference, Stanford, California, August 31-September 2, 1970.

(3) Likins, P. W. and Fleischer, G. E., "Results of Flexible Spacecraft Attitude Control Studies Utilizing Hybrid Coordinates," J. Spacecraft and Rockets., Vol. 8, No. 3 March 1971, pp. 264-273.

NASA — JPL — Comi , L A , Calif